

Simulating land-atmosphere coupling in the Central Valley, California: Investigating soil moisture impacts on boundary layer properties

G. Aaron Alexander^a, Heather A. Holmes^b, Xia Sun^{c,d}, Dani Caputi^e, Ian C. Faloona^e, Holly J. Oldroyd^{*,a}

^a University of California, Davis, Department of Civil and Environmental Engineering, Davis, California, USA

^b University of Utah, Department of Chemical Engineering, Salt Lake City, Utah, USA

^c Cooperative Institute for Research in Environmental Sciences, University of Colorado, Boulder, Boulder, Colorado, USA

^d National Oceanic and Atmospheric Administration, Global Systems Laboratory, Boulder, Colorado, USA

^e University of California, Davis, Department of Land, Air, and Water Resources, Davis, California, USA

ARTICLE INFO

Keywords:

Surface fluxes
Meso-scale numerical simulations
Atmospheric boundary layer
Land surface models
Planetary boundary layer schemes
Evapotranspiration

ABSTRACT

Soil moisture links hydrologic and atmospheric processes and impacts important properties of the atmospheric boundary layer via turbulent land-atmosphere exchange. Research on land-atmosphere interactions and their impacts on the simulated boundary layer in semi-arid regions with substantial irrigation is relatively sparse. We use the Weather Research and Forecasting (WRF) model to evaluate the influence different land surface models (LSMs) and planetary boundary layer (PBL) schemes have on the performance of simulations through comparisons with multi-scale observations during a fifteen-day summertime period during 2016. The focus region for this study is the Central Valley (CV), California, which receives little to no rain in the summer and relies on widespread irrigation for agriculture. Results demonstrate that the LSM drives the differences between simulations, showing only minor variations with changing the PBL scheme. Simulations using the RUC (Rapid Update Cycle) and PX-NO (Pleim-Xu without soil moisture and soil temperature nudging) LSMs generated better comparisons with observed PBL depths. Contrasting RUC however, PX-NO better simulates surface fluxes and humidity, whereas Noah (Noah Unified) and Noah-MP (Noah Multiparameterization) simulate better temperatures despite relatively poor surface flux performance. For most quantities, indirect soil nudging in PX (Pleim-Xu) did not improve results compared to PX-NO, which may be related to soil moisture initialization, the nudging dataset, or a need for model improvements in arid regions. Despite these variations in performance statistics across simulations and quantities, we show that potential evapotranspiration (ET_o) has robust performance statistics across simulations. This suggests that ET_o depends more strongly on net radiation, which performs relatively well across simulations, than on wind, temperature, and humidity, and indicates a further disconnect between ET_o and latent heat fluxes in WRF simulations. Finally, we suggest strategies to obtain the necessary observations to better understand the multi-scale dynamics in the CV and drive subsequent model development.

1. Introduction

Nonlinear physical processes relating conditions of the land-surface with the overlying atmosphere drive the partitioning of available surface energy and surface exchanges through heat, momentum, and water vapor fluxes (Wyngaard, 2010). Through land-atmosphere coupling, soil moisture is a critical component that links the surface hydrologic and atmospheric systems. For example, soil moisture impacts precipitation (Ford et al., 2015; Koster et al., 2004; Welty and Zeng, 2018; Zhang

et al., 2008), near-surface meteorology (Berg et al., 2014; Gevaert et al., 2018; Kala et al., 2015; Schwingshackl et al., 2017; Sun et al., 2017), intensification of droughts (Basara et al., 2019; Christian et al., 2019; Fernando et al., 2016; Leeper et al., 2017; Zaitchik et al., 2013), and evolution of the planetary boundary layer (PBL) height and structure (Dirmeyer and Halder, 2016; Santanello et al., 2018; 2007). Simulating land surface properties, including soil moisture, is complicated and requires parameterizations for the vegetation and soil properties in a numerical grid cell (Ning et al., 2010; Santanello et al., 2018; 2011; 2019),

* Corresponding author.

E-mail address: hjoldroyd@ucdavis.edu (H.J. Oldroyd).

<https://doi.org/10.1016/j.agrformet.2022.108898>

Received 10 September 2021; Received in revised form 11 February 2022; Accepted 1 March 2022

Available online 9 March 2022

0168-1923/© 2022 The Authors. Published by Elsevier B.V. This is an open access article under the CC BY-NC-ND license (<http://creativecommons.org/licenses/by-nc-nd/4.0/>).

often leading to uncertainties in simulating land-atmosphere exchanges. Land-atmosphere exchange processes are typically simulated using a land surface model (LSM) to communicate between land surface properties, or boundary conditions, and the state of the lowest layer of the atmosphere in numerical weather prediction (NWP) models.

LSM performance varies by geographic region and is affected by the sophistication of parameterizations (Van Den Broeke et al., 2018). Regions heavily dominated by agriculture often exhibit large uncertainties due to anthropogenic water and land use. Irrigation and vegetation properties vary in space and time and hence, are difficult to constrain in the LSM (Jackson, 2021). For example, studies of the Central Valley (CV) of California have found that the vast agricultural land-use in the region requires parameterizations in the LSM that impact simulated soil moisture content (Kueppers and Snyder, 2012; Sorooshian et al., 2011; 2012). These parameterizations help account for irrigation, typically reduce model errors of the near-surface meteorology, and range in complexity (see also Section 2.2). While these parameterizations can sometimes improve simulations, they can also create unrealistic conditions in the vadose zone—the region between the soil surface and the water table—for the CV (Sorooshian et al., 2014). A more complex scheme that is based on vegetation greenness during summertime tends to increase the amount of soil moisture and has been shown to lead to increased latent heat flux, decreased sensible heat flux, and increased available energy due to surface cooling and reduced outgoing longwave radiation (Yang et al., 2019). In addition, it may be feasible to include statistical irrigation modeling approaches in WRF (e.g., via Noah-MP by Zhang et al., 2020), however, the necessary data to develop and test these approaches are not available. A relatively sophisticated LSM that includes parameterizations for complex plant physiology and multiple canopy layers improved evapotranspiration estimates in the CV compared to control simulations (Xu et al., 2017). However, a systematic study of how various, widely available LSMs impact atmospheric simulations over the summertime CV using comparisons with a wide range of multi-scale observations is needed to better quantify their respective performance and influences on the atmospheric boundary layer.

In addition to irrigation and soil moisture, the meteorology and wind flow patterns in the CV are complex due to the mountainous terrain, an incoming marine-layer system, and heterogeneous land surfaces (i.e., rapidly changing surface types: urban, rural, vegetation, and savanna). The complex atmospheric processes that occur in the CV have been investigated through modeling, observational, and remote-sensing based studies (Bao et al., 2008; Bianco et al., 2011; Caputi et al., 2019; Faloona et al., 2020; Kueppers and Snyder, 2012; Lawston et al., 2017; Lin and Jao, 1995; Lo and Famiglietti, 2013; Michelson and Bao, 2008; Sorooshian et al., 2014; 2011; 2012; Xu et al., 2017; Yang et al., 2019). Both observations and simulations have shown a decrease in near-surface air temperature over regions of agricultural land-use due to increased evapotranspiration. Additionally, observations in the CV showed that summertime irrigation increased the near-surface soil moisture over agricultural land and changed localized land-surface parameters, such as albedo, which Bianco et al. (2011) suggest may influence large-scale effects generating lower PBL heights compared to other times of the year. Furthermore, Kueppers and Snyder (2012) used a regional climate model to investigate the impact of climate change in the CV and found reduced PBL heights, increased evapotranspiration, weaker near-surface wind speeds, and reduced air temperatures even over nonagricultural locations.

Many land-atmosphere coupling studies focus on their impacts on cloud development and precipitation and therefore, focus their research on regions where precipitation is likely (e.g., Ek and Holtzlag, 2004; Guillod et al., 2015; Hohenegger et al., 2009; Milovac et al., 2016; Santanello et al., 2018; Santanello et al., 2011). This study focuses on the summertime CV, an arid and semi-arid agricultural region having almost no precipitation in the hot summer where soil moisture lost through evapotranspiration can only be replenished by irrigation (Kueppers and

Snyder, 2012). Therefore, we aim to investigate how land-atmosphere coupling and LSMs drive atmospheric boundary layer properties (e.g., Michelson and Bao, 2008), as opposed to precipitation. Due to the lack of summertime precipitation and fertile soils, the CV contains 9.3 million acres of irrigated farmland as of 2015 (Dieter et al., 2018), and it supports more than 250 crop varieties with a value greater than \$20 billion per year (Faunt et al., 2016). Mixed land-use resulting from the spatial distribution of agricultural practices in the CV generates a patchwork of surface conditions and soil moisture that vary considerably throughout the basin (Koster et al., 2019) and that vary temporally depending on irrigation timing and depth. Studies to date have investigated the effects of soil moisture on one component of the atmospheric system in the CV, such as near-surface meteorology (Michelson and Bao, 2008), PBL depth (Bianco et al., 2011; Jackson, 2021; Sorooshian et al., 2011), evapotranspiration (Sorooshian et al., 2012; Xu et al., 2017) or the larger-scale water cycle which can influence precipitation and cloud formation downstream of the CV over Nevada, Utah, and Colorado (Huang and Ullrich, 2016; Lo and Famiglietti, 2013). The goal of this study is to use a regional-scale model to evaluate various combinations of LSM and PBL schemes via comparisons with multi-scale observations in the summertime CV including near-surface meteorology, PBL structure and depth, and turbulent surface fluxes. Since the CV is a semi-arid region with substantial agricultural activity, this paper specifically aims to investigate soil moisture initialization, LSM differences in modeled soil moisture and land-atmosphere coupling, and their subsequent impacts on the atmospheric boundary layer.

Section 2 describes the WRF model configuration, with a focus on how the LSMs simulate soil moisture and surface fluxes. It also provides a brief overview of observations used for comparisons, and model evaluation statistics used in this study. In Section 3, the results and discussion of the LSM and PBL scheme sensitivity testing in WRF are provided and compared to aircraft and/or ground-based observations of turbulent fluxes, near-surface meteorology, boundary layer structure and depth, and potential evapotranspiration (ET_o) estimated from standard meteorological stations. Finally, Section 4 suggests strategies for a comprehensive study to better understand the multi-scale dynamics in the CV and to help drive subsequent model development.

2. Methods

2.1. WRF model configurations

The WRF model is a fully compressible, non-hydrostatic regional atmospheric model (Skamarock et al., 2008). The Advanced Research version of WRF, version 3.8.1, was configured using two, two-way nested domains with 12- and 4-km horizontal resolutions (Fig. 1). Domain 1 (12-km) covers much of the western United States and extends into the eastern Pacific Ocean to include variations of synoptic-scale motions associated with coastal flow patterns, which drive many meteorological processes in the CV (Bao et al., 2008). Domain 2 (4-km) centers on California's CV and is the primary interrogation region for this paper. Simulations used 50 vertical, terrain-following levels, with 30 below 3 km, including 13 levels below 1 km agl (above ground level). The centroid of the lowest grid box was located at 10 m agl. The terrain elevation in Domain 2 ranged from 10 m below sea level to above 4000 m in the Sierra-Nevada Range. The U.S. Geological Survey 28-category land cover dataset was used for land-use information in all the simulations due to its increased agricultural land-use designations in the CV compared to other land-use datasets. The land-use data, which are based on the principal land-use within the numerical grid (Fig. 1), provide important land surface boundary conditions and characteristics, such as aerodynamic resistance and shade fraction.

Simulations were initialized at 00 UTC 24 July 2016 and were run through 8 August 2016, except for the one simulation using the PX LSM, which was initialized on 00 UTC 14 July 2016 to incorporate the indirect soil moisture and temperature nudging, which requires a 10-day spin-up

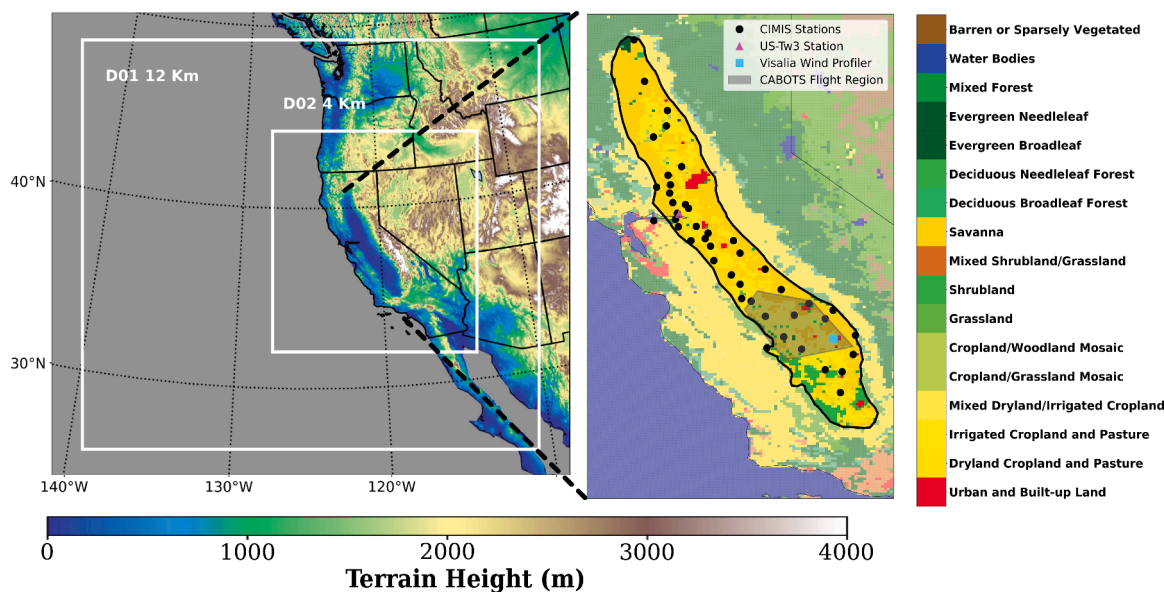


Fig. 1. WRF two-way nested domains at 12 and 4 km with terrain elevation represented in meters. Inlay shows land-use in the interior of the CV, with the California Irrigation Management Information System (CIMIS) stations, the US-Tw3 Ameriflux Station, the wind profiler at Visalia, and the California Baseline Ozone Transport Study (CABOTS) flight domain used for comparisons (see Section 2.4).

period (Pleim and Xiu, 2003; Ran et al., 2015; 2016). The selected analysis period corresponds with available flight data, described below. Simulation times before 25 July 2016, the beginning of the analysis period, were considered to be model spin-up and not used in the analyses. Boundary and initial conditions were from the North American Regional Reanalysis (NARR) with the 3-hourly dataset and 32-km natural grid (Mesinger et al., 2006). NARR was chosen due to its relatively high temporal resolution compared to other reanalysis products for North America. Each simulation used two types of four-dimensional data assimilation, or grid and surface nudging, in Domain 1. Grid nudging above the planetary boundary layer adjusted wind speed and direction, atmospheric moisture, and temperature based on Upper-Air Observational Weather Data (NOAA/NCEP 2004, 2004b). Surface nudging of wind speed and direction, specific humidity, and temperature were provided from the National Centers for Environmental Prediction Global Surface Observational Weather Data and compiled through the OBSGRID program with the Cressman radius of influence scheme (NOAA/NCEP 2004, 2004a; Skamarock et al., 2008).

To address the objectives in this paper, a WRF sensitivity study was designed, specifically varying the WRF schemes that impact land-atmosphere interactions. The WRF simulations compared different combinations of the LSM and PBL schemes are listed in Table 1 which also lists the surface layer scheme for each sensitivity experiment. The other physics options were kept the same in each simulation and are also listed in Table 1 under “Common Model Options”.

2.2. Land surface models

This study uses four LSMs available in the WRF model: Rapid Update Cycle (RUC), Noah Unified (Noah), Noah Multiparameterization (Noah-MP), and Pleim-Xiu (PX) with and without (PX-NO) indirect soil moisture and soil temperature nudging. These LSMs were selected because they vary in the level of complexity and are commonly used in land-atmosphere coupling studies. Within the WRF model framework, the LSM simulates sub-grid processes that occur at or below the land surface, such as energy partitioning, the evolution of soil moisture and soil temperature, snow physics, and the evolution of the surface water budget. For soil moisture, all of the LSMs in this study rely on the same fundamental model, where the vertical distribution of soil moisture is calculated based on the 1-D Richards Equation (Richards, 1931;

Table 1

List of the nine WRF experiments with corresponding Land Surface Models (LSM), Planetary Boundary Layer (PBL) Schemes, and Surface Layer Schemes, in the left four columns. The righttwo columns show the common physics options used in all simulations.

Simulation Naming Convention				Common Model Options	
Model Label	LSM	PBL	Surface Layer Scheme	Category	Option Chosen
ACM2 PX- NO	PX	ACM2	Pleim-Xiu	Microphysics	Morrison Double Moment
ACM2 PX	PX	ACM2	Pleim-Xiu	Longwave Radiation	RRTMG Longwave Scheme
ACM2 RUC	RUC	ACM2	Revised MM5 Scheme	Shortwave Radiation	RRTMG Short- wave Scheme
MYNN RUC	RUC	MYNN 2.5	Revised MM5 Scheme	Cumulus Parameteri- zation	Kain-Fritsch Cumulus
MYNN Noah	Noah Unified	MYNN 2.5	Revised MM5 Scheme	Land Use Table	USGS 28 Catagory
MYNN Noah- MP	Noah- MP	MYNN 2.5	Revised MM5 Scheme	Boundary Conditions	NARR
YSU RUC	RUC	YSU	Revised MM5 Scheme	Model Nudging	FDPA & Observational Nudging
YSU Noah	Noah Unified	YSU	Revised MM5 Scheme		
YSU Noah- MP	Noah- MP	YSU	Revised MM5 Scheme		

Smirnova et al., 1997) and the soil type is assumed to be constant throughout the soil column.

LSMs have a significant impact on the simulated moisture properties with large uncertainties in the hydrological variables, e.g., latent heat flux (LH), humidity, and precipitation. In atmospheric models, the surface energy balance equation is used to prognostically estimate the surface temperature and humidity. In the surface energy balance

equation, the bulk transfer method is used to approximate the surface sensible and latent heat fluxes using the potential temperature and humidity gradients, respectively. There are large differences in the parameterizations of the LH between the different LSMs that are incorporated through evaporation parameterizations. In general, the calculation of the total evaporation in the LSM is split into four different physical mechanisms:

$$E = (E_D + E_C + E_T + E_S), \quad (1)$$

where E_D is the amount of direct evaporation from the soil surface, E_C is the evaporation from water droplets on the canopy surfaces, E_T is the transpiration from the plant canopy and roots, and E_S is the contribution of the snow surface. There is no snow in the CV during August hence, E_S is not applicable to this study. Parameterizations for E_T include a stomatal resistance term. Noah, RUC, PX, and PX-NO use the Jarvis method (see Xiu and Pleim, 2001) which accounts for how radiation stress, soil stress, vapor pressure deficit, and ambient air temperature impact stomatal resistance. In contrast, Noah-MP implements the Ball-Berry Method for stomatal response as described in Appendix B of Niu et al. (2011).

The RUC LSM is different from most LSMs because it uses a thin layer approximation where the surface energy balance equation is applied over a thin layer, defined as the region from the middle of the lowest atmospheric layer to the middle of the first soil layer (Benjamin et al., 2004; Smirnova et al., 1997; 2015). The three other LSMs (Noah, Noah-MP, and PX) incorporate a surface resistance model to estimate the evapotranspiration (E_T). All three of these LSMs use a framework that relies on the resistance analogy to estimate evaporation, where the different resistances represent physical processes in the plant canopy and atmosphere. This framework still relies on the bulk transfer method because the vertical gradient of moisture is used in the evaporation calculation. An aerodynamic resistance accounts for the atmospheric processes and the canopy resistance incorporates parameterizations for the effects of radiation, water stress or vegetation wilting, vapor pressure deficit, and air temperature dependence. Each LSM uses a different formulation to calculate these resistances but Noah, Noah-MP, and PX all start with the simple resistance model in Noilhan and Planton (1989). Noah, the least complex of the three, accounts for stomatal effects in the canopy resistance and updates have added leaf area index (LAI) datasets to improve the physical representativeness of the model (Chen et al., 1996; Ek et al., 2003). Noah-MP starts with the Noah LSM and enhances it by implementing more physically representative mathematical formulations and a framework that allows for multiple implementations of the parameterized physical processes for vegetation versus other land cover in the LSM (Niu et al., 2011; Yang et al., 2011). The PX LSM updates the Noah modeling framework for the surface and canopy resistances, where the soil evaporation equations are updated with a parameter that better accounts for different soil types, and the canopy resistance is updated with a formulation of the stomatal resistance, adding LAI and including a scaling factor to account for shading (Gilliam and Pleim, 2010; Pleim and Xiu, 2003; Xiu and Pleim, 2001).

Two of the LSMs, RUC and PX, include additional methods that aim to improve the soil moisture estimates. These soil moisture modifications have a significant impact in arid regions, especially those with irrigated agricultural land. Specifically, RUC modifies the soil moisture to account for a plant wilting point, which is the soil moisture content where transpiration would stop. The wilting point is a hydraulic parameter that is based on soil type in atmospheric simulations. RUC uses this parameter as cut-off factor by not allowing the soil moisture to be less than 20% above the soil moisture wilting point (Smirnova et al., 1997; 2015). While this method does not directly incorporate irrigation patterns, it can increase the amount of soil moisture for cropland, especially for arid/semi-arid regions.

The PX model modifies soil moisture through two methods: recalculation of vegetation fraction and indirect soil temperature and soil

moisture nudging. It recalculates vegetation parameters, including vegetation fraction, by aggregating them from high resolution (1-km) datasets to set the average grid-cell values (Xiu and Pleim, 2001). The adjusted vegetation fraction modifies surface soil moisture by increasing (decreasing) vegetation fraction, causing decreased (increased) direct evaporation from the soil surface and increased (decreased) losses to the lower soil layer (Pleim and Xiu, 2003; Xiu and Pleim, 2001). Additionally, the PX model features the option for indirect soil moisture and soil temperature nudging in both soil layers (Pleim and Gilliam, 2009; Pleim and Xiu, 2003). The indirect soil nudging uses the weighted differences between simulated surface air temperature and relative humidity and observational or assimilated data, with the aim of reducing biases (Pleim and Gilliam, 2009; Pleim and Xiu, 2003). Specific information regarding the data assimilation WRF used for indirect soil moisture and soil temperature nudging for this study of the CV is provided in the Supplemental Material.

2.3. Planetary boundary layer schemes

The three PBL schemes used in this study include the Mellor-Yamada Nakanishi Niino (MYNN) 2.5 scheme, a 2.5-order local closure scheme with turbulence closure constants that are tuned using a database of large-eddy simulation results (Cohen et al., 2015; Nakanishi and Niino, 2004; 2009); the Yonsei University (YSU) scheme, a first-order, non-local closure scheme with a counter-gradient flux term for scalar mixing and an explicit treatment of the entrainment zone (Hong et al., 2006); and the Asymmetric Convection Model 2 (ACM2) scheme, a hybrid local and non-local first-order closure scheme featuring a weighted counter-gradient flux correction term that increases in intensity near the surface (Pleim, 2007a; 2007b). To couple the LSM and PBL schemes, two surface layer schemes, the revised MM5 and PX, were used in this study. They differ only by the addition of a parameterization of the viscous sub-layer that is modeled using a quasi-laminar boundary layer resistance in PX (Jiménez et al., 2012; Pleim, 2006). All model combinations are listed in Table 1, where 'ACM2 PX-NO' indicates that indirect soil moisture and soil temperature nudging options were not used, whereas ACM2 PX implemented the nudging with a ten-day spin-up.

Each PBL scheme uses a different method to compute the PBL heights, based either on bulk Richardson numbers or turbulence kinetic energy (Sathyanadh et al., 2017). To use a common PBL metric across simulations, the PBL heights were recalculated using profiles of the bulk Richardson number, where the PBL height is designated as the vertical level where the Richardson number crosses a critical value, $Ri_b = 0.2$, following Zhang et al. (2014) and Sun et al. (2017).

2.4. Observations

Comparisons with a suite of multi-scale observations were used to evaluate simulation results. Near-surface observations of two-meter air temperature (T2), two-meter dew point temperature (Td2), two-meter wind speed (WS2), and potential evapotranspiration (ETo) were obtained from the California Irrigation Management Information System (CIMIS) stations. CIMIS stations measure relevant meteorological variables, reported hourly, to estimate potential evapotranspiration for agricultural practices based on the 'CIMIS Penman' equation, a Pruitt-Doorenbos modified Penman equation (Pruitt and Doorenbos, 1977), which incorporates a weighting function between net radiation and a vapor pressure deficit wind function with unique cloud factor values for each station location (California Department of Water Resources, 2021; Dong et al., 1992). Forty-one CIMIS stations at sites with diverse land-use, including fallow fields, low lying shrubs, and annual crops, were active within the CV during the simulation period (see Fig. 1). Due to instrumentation sensitivity and limitations, 102 CIMIS data points were removed during the study period, amounting to less than one percent of the number of points used for comparisons. WRF

does not directly calculate two-meter wind speeds (WS2), therefore Monin-Obukhov similarity theory and the simulated ten-meter wind speed were used to extrapolate for WS2 comparisons (see details in the Supplemental Materials).

Additionally, surface turbulent fluxes (via eddy-covariance methods) and soil moisture measurements from the Ameriflux Twitchell Island 3, listed as US-Tw3, in the Sacramento-San Joaquin River Delta (latitude: 38.1159N, longitude 121.64666W, elevation: -9 m relative to sea level) served as a dataset for comparisons with simulations (Oikawa et al., 2017). The flux station is located over an alfalfa field that uses sub-surface irrigation throughout the dry summer, and the eddy-covariance sensors are mounted at 2.8 m agl. Within WRF simulations, this site is designated irrigated cropland.

Airborne measurements from the California Baseline Ozone Transport Study (CABOTS) (Faloona et al., 2020) provided observations of potential temperature and specific humidity profiles. Daytime CABOTS flights took place during the afternoons (11:00 and 16:00 PST) on 27–29 July 2016 and 04–06 August 2016, which correspond to the so-called ‘EPA Flights’ during the full CABOTS campaign (Faloona et al., 2020).

PBL heights determined from bulk Richardson number analyses (see Section 2.3) of individual potential temperature and specific humidity profiles were temporally averaged through the period of active growth (i.e., 11:00–16:00 LST) and spatially averaged within the shaded region in Fig. 1 for comparison with WRF simulations. These measurements act as a bulk estimate of the PBL heights within San Joaquin Valley. Further information on the methodology used to collect this dataset can be found in Caputi et al. (2019), Trousdell et al. (2019), and Faloona et al. (2020). Finally, afternoon comparisons of vertical profiles of wind speed and direction use in-situ measurements from a 915 MHz wind profiler near Visalia, CA (latitude: 36.31N, longitude -119.39W, elevation: 81 meters). This profiler measures hourly averaged wind speed and direction from near the surface to approximately 1 km agl and is part of the National Oceanic and Atmospheric Administration Earth Systems Research Laboratories (NOAA-ESRL) network of sensors throughout California.

2.5. Model evaluation metrics

Near-surface meteorological variables (T2, Td2, WS2, and ETo) in

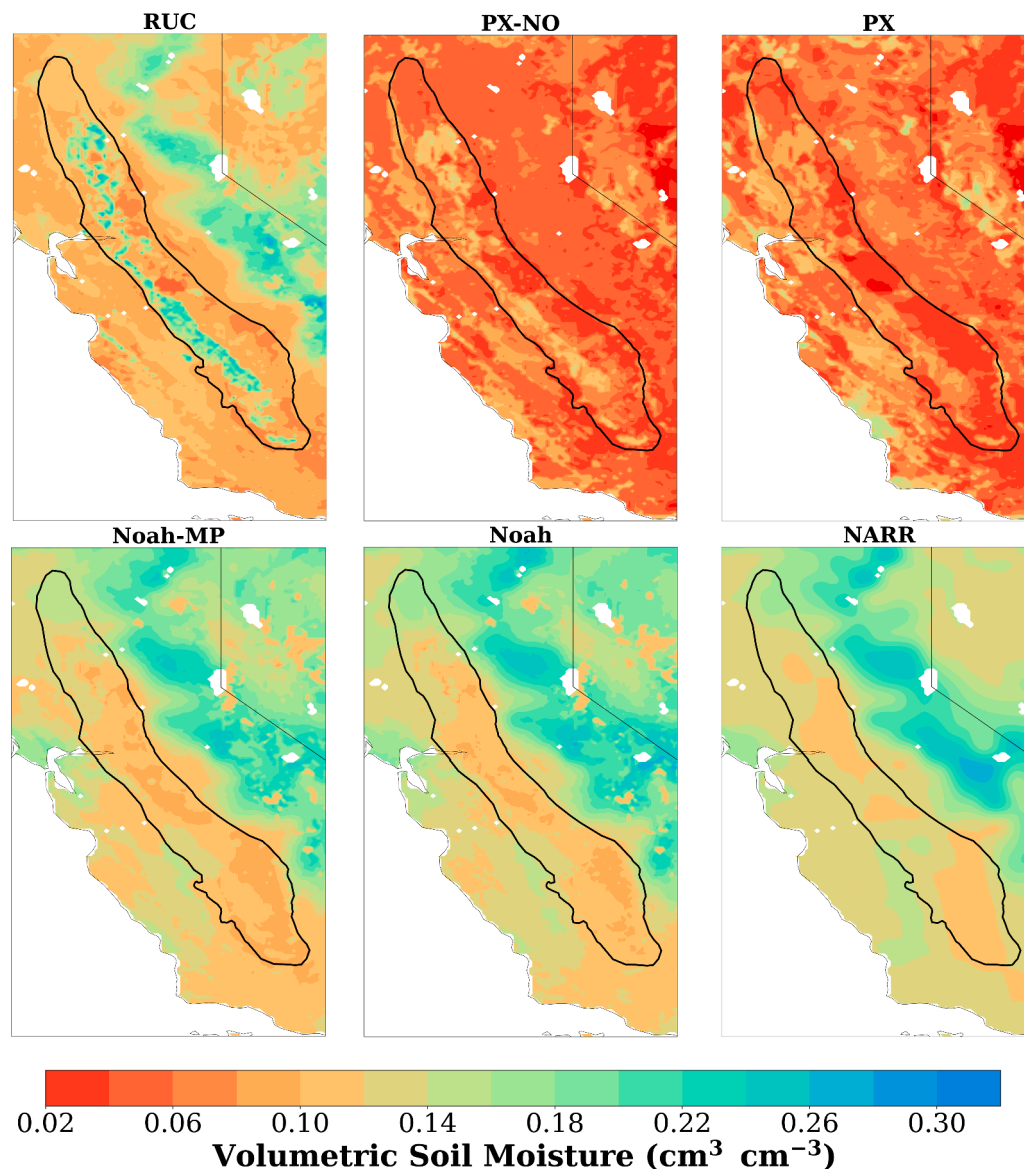


Fig. 2. Simulated top layer soil moisture averaged between 25 July 2016 00 UTC to 08 Aug 2016 00 UTC from MYNN RUC (0 cm), ACM2 PX-NO (0.5 cm), ACM2 PX (0.5 cm), MYNN Noah-MP (5 cm), and MYNN Noah (5 cm) WRF simulations with initialization conditions (NARR reanalysis dataset). The Central Valley is outlined in black on all panels.

the CV and time series statistics of surface turbulent fluxes were compared with respective observations through calculation of the Mean Bias (MB), Index of Agreement (IOA), the Mean Absolute Error (MAE), and the Root Mean Square Error (RMSE). MB is an unbounded metric, with negative values describing an underestimation compared to observations, and positive values corresponding to an over-estimation. The optimal value MB is zero, indicating perfect agreement between simulated and observed values. MAE and RMSE are a measure of agreement between simulated and observed values bounded between 0 and $+\infty$, with the point of optimality at zero. Finally, IOA is an additional statistic to detect the differences between simulated and observed values, bounded by 0 and 1. The IOA is sensitive to outliers due to the squared difference in both the numerator and denominator. The respective mean, standard deviation (STD), and median (MED) values are also provided. Evaluation statistics are mathematically defined in the Supplemental Material.

3. Results and discussion

3.1. Soil moisture

Figure 2 shows the simulated mean volumetric soil moisture fields from the top soil layers in WRF and NARR that were used for initial conditions. All data were averaged temporally over the analysis period (25 July 2016 at 00 UTC to 8 August 2016 at 00 UTC). Soil moisture fields differ by less than 2% by changing the PBL schemes for a given LSM, so only results from the ACM2 and MYNN PBL schemes are shown for the various LSMs and YSU results are not shown. Across all LSMs, the highest soil moisture is located over a patchwork along southwest edge of the southern CV and in northern portions of the CV in the regions designated as irrigated cropland or mixed dryland/irrigated cropland in Fig. 1, hereafter called ‘cropland’. Most of the rest of the CV is designated as savanna and is relatively drier. This is most prominent in the RUC LSM, for which soil moisture is approximately $0.24 \text{ cm}^3 \text{ cm}^{-3}$ in the cropland regions, or more than double compared to those from Noah, Noah-MP, and the NARR initialization. The PX-NO simulation shows the second highest soil moisture values in the cropland regions, approximately $0.15 \text{ cm}^3 \text{ cm}^{-3}$. However, both PX and PX-NO are drier elsewhere, and the PX simulation produces the driest fields overall. For these cases, the direct effect of soil moisture nudging in the PX simulation was to generate lower soil moisture values compared to the PX-NO simulation, especially for cropland. This is a surprising result. Given the high amounts of irrigation applied to grow crops in the otherwise arid agricultural lands of the CV, the tendency for the simulations to

underestimate soil moisture (Fig. 3), and the challenges associated with constraining irrigation in models, we expected PX to produce higher soil moisture values than PX-NO. PX also produced a drying effect from initial conditions (NARR), even in the cropland regions.

In addition, the PX, PX-NO and RUC simulated soil moisture fields exhibit larger spatial variability, which likely reflects their additional parameterizations for croplands that aim to generate improved soil moisture estimates, as discussed in Section 2.2. In these WRF simulations, the treatment of soil moisture affects both spatial heterogeneity and the range of soil moisture values that occur. In contrast, Noah and Noah-MP exhibit only slightly more variability than the initial conditions, which likely reflects the simulations having higher spatial resolution than the NARR reanalysis data. The soil moisture values from Noah and Noah-MP are similar to NARR with only slightly higher values in the cropland regions.

Time series of soil moisture were also analyzed to compare temporal trends between LSMs and to compare with the available in-situ observations at the US-Tw3 Ameriflux site (Fig. 3). In general, a dearth of publicly available soil moisture data, especially in the CV, limits comparisons with observations for agricultural lands to the single site. The uppermost observation levels at US-Tw3 (10 cm and 20 cm) are shown with the simulated values from the available top soil layer from each LSM (RUC: 0 cm, PX: 0.5 cm, Noah/Noah-MP: 5 cm). The US-Tw3 site receives sub-surface irrigation in summer. However, no irrigation signal (i.e., a significant increase in observed soil moisture) is visible at either depth during the study period nor in multi-year time series of soil moisture during the summertime (not shown). Given the challenges associated with comparing a model grid cell to a single point measurement and the differences in the physical locations for the top layer between simulations, comparisons of soil moisture values are somewhat qualitative. In general, these comparisons show that the time series reflect differences between LSMs seen in the averaged fields for cropland in the CV (Fig. 2). More prominently, they show that the simulated values are lower than those observed, which may indicate two things: (i) that the LSMs underestimate irrigation soil moisture in croplands, even those with additional parameterizations designed to improve soil moisture estimates, and (ii) that despite these underestimations, soil moisture nudging in PX produces drier soil than PX-NO. Noah and Noah-MP show a clear drawdown signal and produce very similar values. PX-NO also exhibits a drawdown trend, though less strongly toward the end of analysis period, and the observations show a slight moisture drawdown. Uniquely, the RUC simulation shows no temporal variability due to the cropland parameterization in the RUC model for which the soil moisture is not allowed to be lower than 20% above the soil moisture

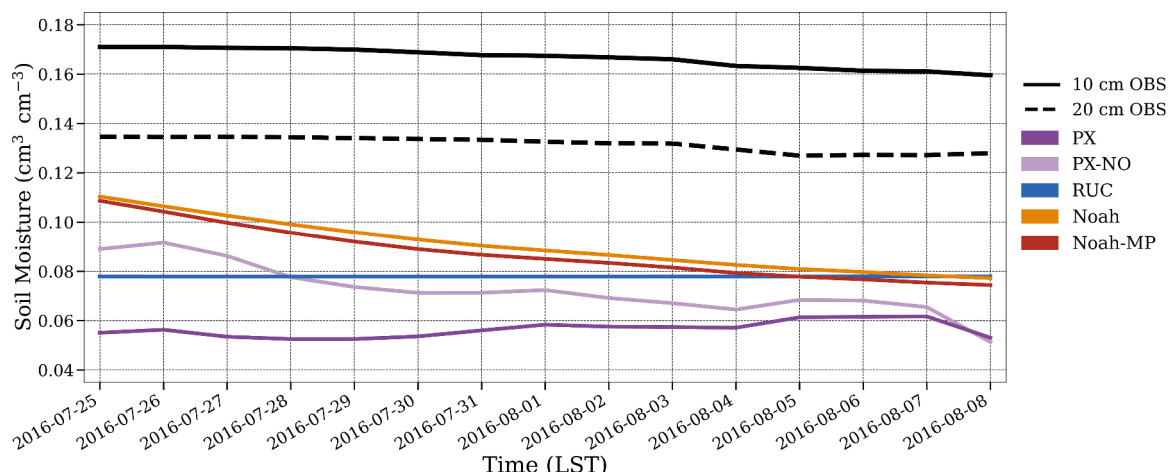


Fig. 3. Time series of daily mean soil moisture from 25 July 2016 to 08 August 2016 showing the top two soil moisture measurements (10 cm and 20 cm) from in-situ observations at the US-Tw3 Ameriflux site compared to the top soil moisture layer from MYNN RUC (0 cm), MYNN Noah (5 cm), MYNN Noah-MP (5 cm), ACM2 PX (0.5 cm), and ACM2 PX-NO (0.5 cm) from WRF. Timestamp tick marks indicate midnight.

that corresponds to the vegetation wilting point. In other words, RUC, despite showing the highest values for croplands in Fig. 2, produces only the minimum value possible for the vegetation. Finally, PX shows a very slight increase in soil moisture toward the end of the period, which likely corresponds to the nudging adjusting to a new synoptic setup (see Supplemental Material) but could also indicate a need for longer spin-up time.

While these LSMs have been shown to be successful in simulating soil moisture in a variety of scenarios (Ek et al., 2003; Gilliam and Pleim, 2010; Niu et al., 2011; Smirnova et al., 2015), none of these studies focus specifically on irrigated cropland in the CV where available observational soil moisture data are sparse. Furthermore, most of these studies focused on the midwestern or eastern U.S.A. regions which are much less arid compared to the summertime CV. However, some studies have shown that Noah tends to over-estimate soil moisture in regions with observed low soil moisture, much like the non-irrigated regions of the CV, and under-estimate soil moisture in areas of observed high soil moisture, like the irrigated regions of the CV (Fan et al., 2011; Xia et al., 2015). The comparisons to other studies indicate that LSMs performance in simulating soil moisture will vary by region. Hence, an increase in publicly available soil moisture observations in this region is crucial step toward improving LSM performance. It is worth mentioning that satellite remote sensing products for the CV (not shown), specifically, the Soil Moisture Active-Passive (SMAP) L2, L3, and L4 (O'Neill et al., 2019; Reichle et al., 2018), show even lower soil moisture values than PX during the same time period. Since they were lower values and also require a degree of modeling, we determined that they are not a good comparative reference for this study. This highlights that improving satellite remote sensing for this region is an important area of research needing more attention and surface observations for verification.

3.2. Surface turbulent fluxes

3.2.1. Time series comparison

Figure 4 shows time series comparisons of surface H, surface LH, ground heat flux (G), and net radiation (R_n) between observations from the US-Tw3 Ameriflux station, and those from the nine WRF simulations (Table 1). For the purposes of this study, observed R_n is defined to be the sum of LH, H, and G to make direct comparisons with the WRF simulations for which R_n is partitioned between only these three components. Corresponding evaluation statistics computed between observations and simulations are shown in Table 2.

From the US-Tw3 station, observed turbulent flux partitioning was dominated by LH, which peaked around 400 Wm^{-2} during much of the simulation period. Observed H peaked during the day near 100 Wm^{-2} throughout most of the simulation period but increased to daily maximums of over 200 Wm^{-2} in the last three days of the analysis period, corresponding to a stark decrease in LH maximums (180 Wm^{-2}) and a subsequent flip in Bowen ratios (not plotted directly). At daily scales, the observed H moved from positive to negative in the early afternoon, which is likely due to well-watered crops and the dominance of the LH according to Stull (1988). Observed G peaked in magnitude, $\approx 75 \text{ Wm}^{-2}$, near the times of maximum R_n and slowly decreased throughout the night. Observed R_n typically followed a diel pattern with a fairly consistent peak approaching 600 Wm^{-2} . Given the rare cloud formation over the CV during summertime, variations in observed R_n and the general overestimations of R_n from the simulations may be due to the smoke plume from the Soberanes Fire (Langford et al., 2020).

The simulated surface fluxes at the grid cell containing the US-Tw3 station were highly insensitive to changing the PBL scheme and similar to the soil moisture, variations between simulations correlate with changing LSMs (see Table 2 and Fig. 4). In comparison to the observations, the best performing simulation, by far, is the ACM2 PX-NO (lowest RMSE, MAE and MB in Table 2), which tends to over-estimate daytime LH during much of the analysis period by an average of 58.2 Wm^{-2} and with a maximum over-estimation of 340.7 Wm^{-2} . Noah,

RUC, and PX simulations all underestimated LH by $\approx 100 - 200 \text{ Wm}^{-2}$ with high RMSE, MAE, and negative MB. The overestimate from PX-NO in the first three days could be related to higher than observed R_n , potentially due to differences in atmospheric transmissivities, because H and G compare well during this period. The last three days of the simulation present an exception, for which observed LH from PX-NO drops, and simulations using RUC and Noah produce the best results.

Noah-MP simulations of LH tend to plateau during the day (07–19 LST), which lacks a physically-viable explanation. They leveled off to LH values of about 70 Wm^{-2} , an average underestimation of -163.6 Wm^{-2} , and produce the worst summary statistics by a substantial margin (Table 2). In general, the CV is a moisture-limited evaporative system, meaning that the partitioning of energy to latent heat is limited by soil moisture availability as opposed to available energy (Koster et al., 2004; Santanello et al., 2011). However, relatively dry soil conditions simulated by the Noah-MP LSM were not the primary reason for the poor performance in its LH estimates, given that Noah produces a similar soil moisture field (Figs. 2 and 3). Instead, model parameters are likely a significant factor. Since the soil resistance used in Noah-MP is identical to that in Noah, the simulated behavior in LH is likely caused by the stomatal parameterization (see Niu et al., 2011), for which Noah-MP's implementation is different from all of the other LSMs (Section 2.2).

Simulation evaluation statistics for H are similar to those of LH, with the worst estimates compared to observations generated from the Noah-MP LSM, followed by the RUC LSM, the Noah LSM, and the PX simulation, and with the best H results generated by PX-NO simulation (Fig. 4B and Table 2). PX-NO simulates H especially well over the first four days, and the degradation in model performance might be due to the long simulation length, the change in synoptic set up, or a combination of the two. All LSMs over-estimated H, including PX-NO, on most days. The Noah-MP simulations over-estimated daytime H peaks by as much as nine times but more typically, by about four times, seemingly compensating for its plateau in LH in the energy flux partitioning. The observed afternoon drop toward negative H was not simulated with most of the LSMs until significantly later in the evening, closer following the trends in R_n . In general, the simulated nighttime H values are larger (closer to zero) than the observations. Noteworthy exceptions are the positive H values produced by PX on several nights; these, along with the high daytime H peaks indicate that the soil moisture nudging scheme tends to produce worse results compared to those from PX-NO simulations.

Simulated G and R_n were typically too high during the daytime and too low during the nighttime (Fig. 4C and D, respectively). The Noah-MP simulations over-estimated the variability of the observed G, with standard deviations of $\approx 70 \text{ Wm}^{-2}$ compared to an observed $\approx 30 \text{ Wm}^{-2}$. Simulations with RUC exhibit similar but less extreme behavior, whereas PX and PX-NO tend to under-estimate G, with a notable day for which the G from PX never becomes positive. Simulations that used the Noah LSM most closely matched the observed G, with the most significant differences resulting from an over-cooling during nighttime, and small differences in estimated daytime maximums. Despite the generally poor performance across the simulations for the individual components of the surface energy budget, results for the summed R_n tend to match observed R_n comparatively more closely (peak differences of $\sim 100 \text{ Wm}^{-2}$).

3.2.2. Spatial distributions of turbulent surface fluxes

Spatial variability of afternoon-averaged (11–16 LST) simulated LH and H (Fig. 5) are analyzed to investigate correlations with land-use designation, the spatially distributed soil moisture, and PBL depth (later, in Section 3.3) from each LSM. Again, negligible differences in these fields are associated with changing the PBL scheme (see Fig. 4 and Table 2). This was further verified by the two-sample Kolmogorov-Smirnov test which showed that the choice of the PBL scheme is statistically insignificant. Therefore, Fig. 5 shows only results for the same LSMs as in Fig. 2.

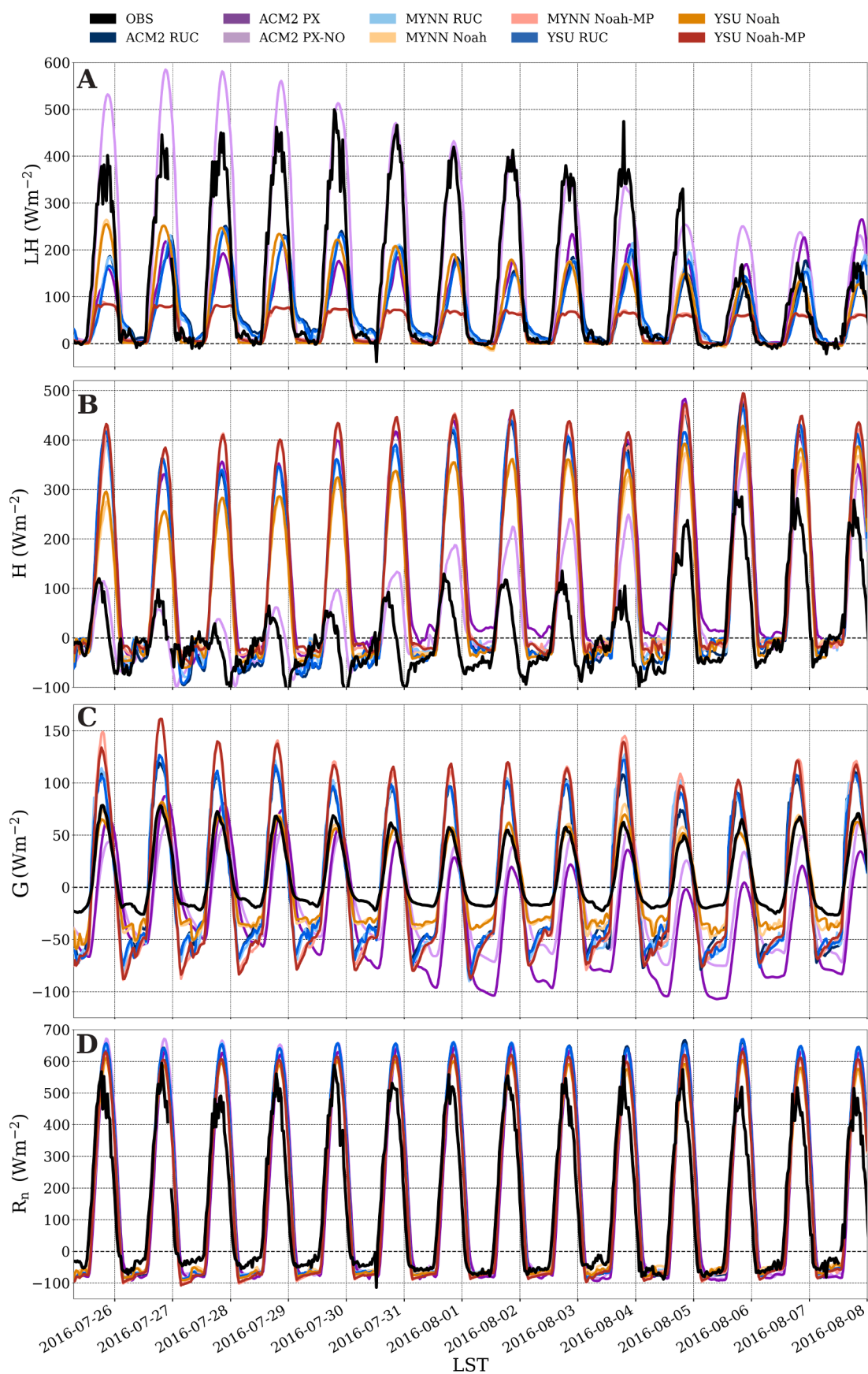


Fig. 4. Thirty-minute averaged time evolution of sensible heat flux (H), latent heat flux (LH), ground heat flux (G), and net radiation (R_n), defined to be the sum of other three panels, comparing the simulated quantities to observations from US-Tw3 Ameriflux from 25 July to 8 August 2016. Timestamp tick marks indicate midnight.

Table 2

Summary statistics calculated between observed Latent Heat Flux (LH), Sensible Heat Flux (H), Ground Heat Flux (G), and Net Radiation (R_n), defined to be the sum of the previous three, and estimates from WRF simulations at the US-Tw3 Ameriflux Site.

PBL:	ACM2			MYNN			YSU			OBS	
LSM:	PX-NO	PX	RUC	RUC	Noah	Noah-MP	RUC	Noah	Noah-MP		
					LH (Wm^{-2})						
Mean:	154.9	65.9	72.8	69.5	67.2	33.4	70.5	66.1	32.8	124.7	
STD:	173.1	72.7	67.5	69.9	79.0	30.6	67.1	78.0	30.6	144.8	
MED:	72.0	30.1	46.1	42.4	24.8	22.6	44.5	23.0	21.9	49.9	
MB:	29.4	- 59.0	- 52.1	- 55.5	- 57.8	- 91.4	- 54.5	- 58.8	- 92.0	-	
MAE:	51.2	74.1	80.0	78.3	63.6	95.2	80.0	64.4	95.5	-	
RMSE:	79.8	114.1	115.7	116.4	97.7	150.9	117.6	99.0	151.0	-	
					H (Wm^{-2})						
Mean:	42.5	135.6	108.8	112.3	95.3	125.1	118.9	96.5	127.8	9.3	
STD:	108.7	161.4	170.5	162.0	141.0	170.4	168.3	147.5	173.7	84.0	
MED:	- 8.1	48.1	11.1	7.7	3.6	16.7	8.0	6.2	25.2	- 14.2	
MB:	33.5	126.2	99.2	102.8	85.8	115.4	102.3	87.0	118.1	-	
MAE:	54.9	131.8	115.8	113.7	94.4	123.6	116.5	97.0	126.7	-	
RMSE:	76.6	184.1	168.2	166.3	139.4	184.2	169.3	143.3	187.6	-	
					G (Wm^{-2})						
Mean:	- 16.1	- 31.4	- 1.4	- 1.9	- 1.2	2.7	- 1.4	- 0.9	2.0	8.9	
STD:	40.5	50.6	60.6	64.4	40.4	71.8	62.0	38.4	70.4	30.8	
MED:	- 26.3	- 42.4	29.4	29.0	11.3	- 33.7	29.1	11.5	- 34.7	- 6.3	
MB:	- 25.0	- 40.3	- 10.3	- 10.8	- 10.1	- 6.2	- 10.3	- 9.8	- 6.9	-	
MAE:	29.1	45.1	80.3	83.9	62.6	39.0	81.6	60.8	37.8	-	
RMSE:	33.9	51.2	91.1	94.6	71.4	43.0	92.4	69.0	41.7	-	
					R_n (Wm^{-2})						
Mean:	181.3	170.2	183.0	183.7	163.7	161.3	183.8	163.6	162.5	142.9	
STD:	279.2	272.4	280.9	278.3	252.1	265.0	279.9	255.9	267.4	217.8	
MED:	37.9	27.4	61.7	54.4	43.7	33.7	59.7	50.8	38.4	20.2	
MB:	37.9	26.9	39.8	40.5	20.5	18.1	40.6	20.4	19.4	-	
MAE:	101.5	103.1	87.1	85.6	69.6	75.7	86.7	71.7	77.4	-	
RMSE:	135.5	132.9	118.1	117.1	92.7	96.7	118.3	94.7	98.8	-	

The PX-NO and RUC simulations produced the highest LH fields (PX-NO average: $223.46 Wm^{-2}$, RUC average: $147.14 Wm^{-2}$) during the afternoon throughout the CV, with several pockets of higher LH (over $400 Wm^{-2}$) in many sub-regions generally designated as cropland. Noah and Noah-MP simulations produced much lower mean LH fields ($78.1 Wm^{-2}$ and $55.36 Wm^{-2}$, respectively) and it appears that the plateauing behavior exhibited by Noah-MP at the US-TW3 site (Fig. 4A) similarly occurs throughout the CV. Cropland regions are generally associated with higher LH, which correlate with the soil moisture fields in RUC and PX-NO (Fig. 2) and generally, but do not necessarily, correlate with soil moisture fields for Noah and Noah-MP. In addition to the regions of elevated LH discussed previously, the PX-NO simulation also produces a region in the southern CV, approaching the eastern boundary exhibiting some of the highest LH values across all simulations. The land-use of this region is also cropland but has relatively lower soil moisture than the other high LH cropland regions. This suggests that while land-use designation and soil moisture are important in driving LH in PX-NO, there are additional variables, model components, or physics that also play an important role. The PX LSM produces the only LH spatial distribution that does not readily appear to directly correlate with the cropland regions or soil moisture and instead, has sparse, relatively high LH patches near the southwest CV boarder. This pattern may be linked to some regional climatic differences as the soil nudging schemes aim reduce MB in the localized temperature and humidity values, however, similar patterns are not visible in the PX soil moisture field.

Simulated spatial distributions of H essentially invert those of LH throughout the CV, where locations with high (low) LH correspond to low (high) H for the same period (Fig. 5). This reflects the partitioning of H and LH as the two dominating non-radiative components in the surface energy budget (see also Fig. 4). Noah-MP produced the highest average H at $393.81 Wm^{-2}$ followed by PX with $345.73 Wm^{-2}$, Noah with $337.70 Wm^{-2}$, RUC with $292.98 Wm^{-2}$, and PX-NO with $286.21 Wm^{-2}$. Even though RUC produced a relatively low average H, it exhibits areas with some of the highest H values, typically for regions designated as savanna in Fig. 1. This exemplifies the significance of the

additional parameterizations that RUC implements for cropland designations, and that without them, the soil moisture, LH and H fields might be more like those from Noah.

3.3. Planetary boundary layer height & structure

PBL heights determined from the critical bulk Richardson number for the WRF simulations compared with those derived from the potential temperature and relative humidity profiles from the CABOTS flights are shown in Fig. 6 for the days with available flight data (see Section 2.4). The mean observed daytime PBL heights, ≈ 550 m agl, agree well with the analyses from Bianco et al. (2011) and Jackson (2021). However, all WRF simulations over-estimated PBL heights for each of the CABOTS flight days. The ACM2 PX-NO simulation produced the best PBL height estimates (within 29% of observations) for the July flights but increase to nearly a factor of 2 larger for the August flights, when RUC simulations tend to perform slightly better. In contrast, the ACM2 PX simulation with indirect soil nudging generated PBL heights that are over double those observed. Comparing ACM2 PX and ACM2 PX-NO PBL heights indicate that the relatively poor surface fluxes from PX propagate to upper levels and significantly impact PBL heights. Simulations with the RUC LSM over-estimated PBL heights by 71% on average compared to observations, while Noah and Noah-MP simulations over-estimated by 140% on average. The most extreme cases, from Noah and Noah-MP, are larger than observed quantities by a factor of \approx three.

PBL heights simulated with the YSU PBL scheme are higher by 10% on average than those generated by the MYNN PBL scheme. When comparing across RUC LSM simulations, the MYNN RUC estimated the lowest PBL heights, the ACM2 RUC simulations estimated 8% higher PBL compared to the MYNN RUC simulations, and the YSU RUC simulations estimated 12% higher than MYNN RUC. Non-local closure schemes, such as the YSU PBL scheme, tend to over-deepen simulated PBL heights in convective regimes compared to local closure schemes (e. g., the MYNN PBL scheme) due to increased propagation of large-scale eddies throughout the PBL, as also shown by others (Cohen et al.,

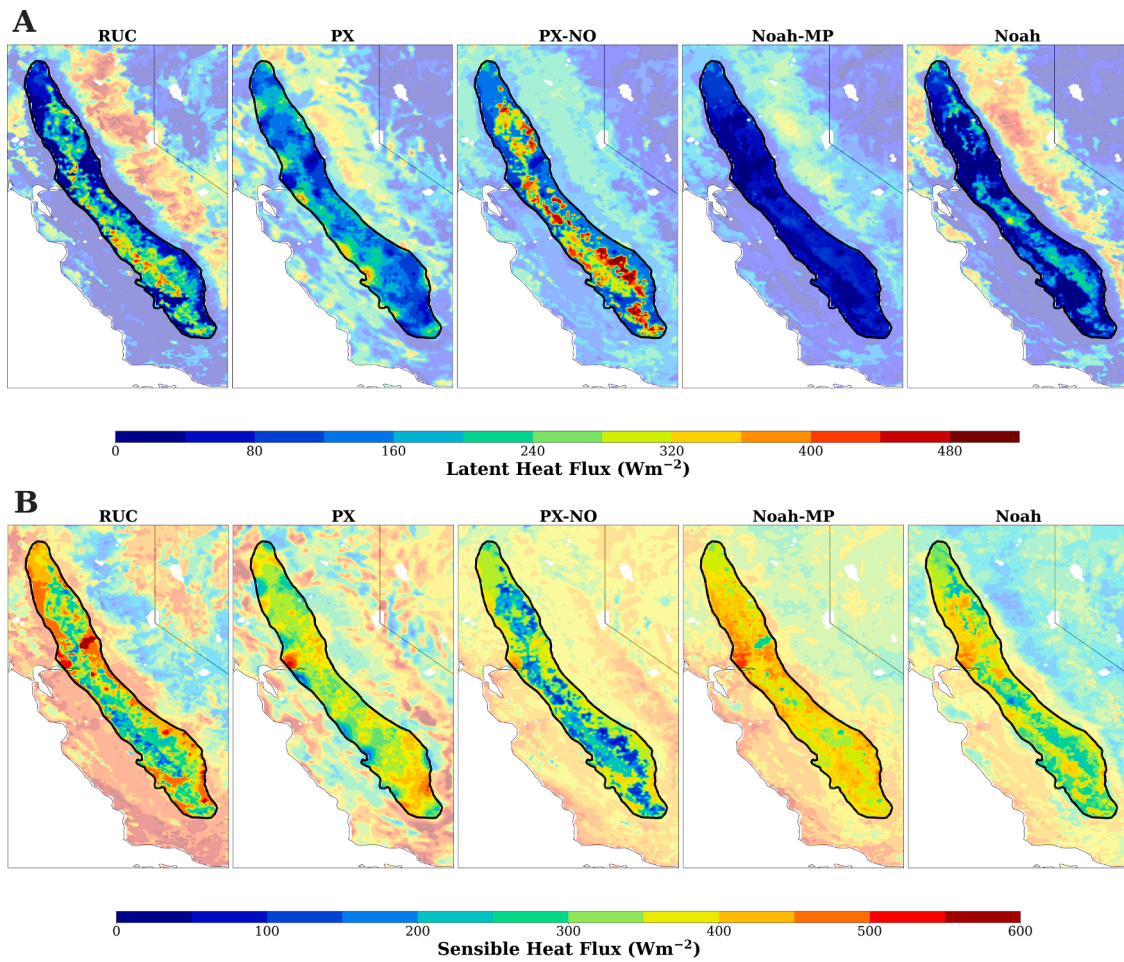


Fig. 5. Afternoon (11-16 LST) averaged a) latent heat flux and b) sensible heat flux at 4-km resolution in the Central Valley from (left to right) MYNN RUC, ACM2 PX, ACM2 PX-NO, MYNN Noah-MP, and MYNN Noah simulations. Boundaries of the Central Valley are outlined in black.

	MYNN RUC	MYNN Noah	MYNN Noah-MP	YSU RUC	YSU Noah	YSU Noah-MP	ACM2 RUC	ACM2 PX-NO	ACM2 PX	OBS
2016-07-27	855	1308	1251	1005	1451	1526	972	615	1338	541
2016-07-28	813	1127	1065	924	1190	1275	881	628	1175	512
2016-07-29	836	1241	1159	950	1290	1391	915	634	1210	492
2016-08-04	1024	1322	1343	1097	1367	1386	1028	1070	1270	645
2016-08-05	959	1176	1138	1064	1235	1291	1027	1104	1242	511
2016-08-06	1055	1239	1191	1150	1293	1340	1159	1216	1278	547

Fig. 6. Daily afternoon (11-16 LST) averaged PBL heights (m agl) from WRF simulations over the CABOTS flight domain estimated from the critical bulk Richardson number compared to flight observations that were available for the 27 to 29 July and 4 to 6 August 2016. Simulated PBL heights closer to observations (rightmost column) correspond to lighter colors.

2015; Sathyanadh et al., 2017).

Though there are significant differences in PBL height that arise from changing the PBL schemes, the results in Fig. 6 show that again, the LSM drives most of the differences between simulation results. Generally, the simulations with relatively higher (lower) patches of LH (H) within the CABOTS domain more closely estimated the observed PBL heights (Bianco et al., 2011; Jackson, 2021). Excluding PX simulations, these relatively low simulated PBL heights are linked more to the LSMs with modified parameterizations for soil moisture, than to the actual soil moisture values, recalling that Noah and Noah-MP have higher soil moisture than PX-NO. This may imply that the surface flux parameterizations specific to each LSM, mainly the evapotranspiration (ET)

parameterizations, play a significant role. For example, Jackson (2021) found that simulated PBL heights in the CV during the summer are significantly reduced by adding extra moisture to the soil boundary condition. However, other idealized studies (e.g., Patton et al., 2005 and Rihani et al., 2015) have linked the variability in soil moisture to improved regional-scale dynamics as it produces more ‘realistic’ variations in localized pressure gradients allowing the formation of convective structures that contribute to the total vertical temperature and moisture fluxes.

Further investigations of the mean PBL structure compares vertical profiles of wind speed, wind direction, potential temperature, and specific humidity to observations (Fig. 7). Observations of wind speed and

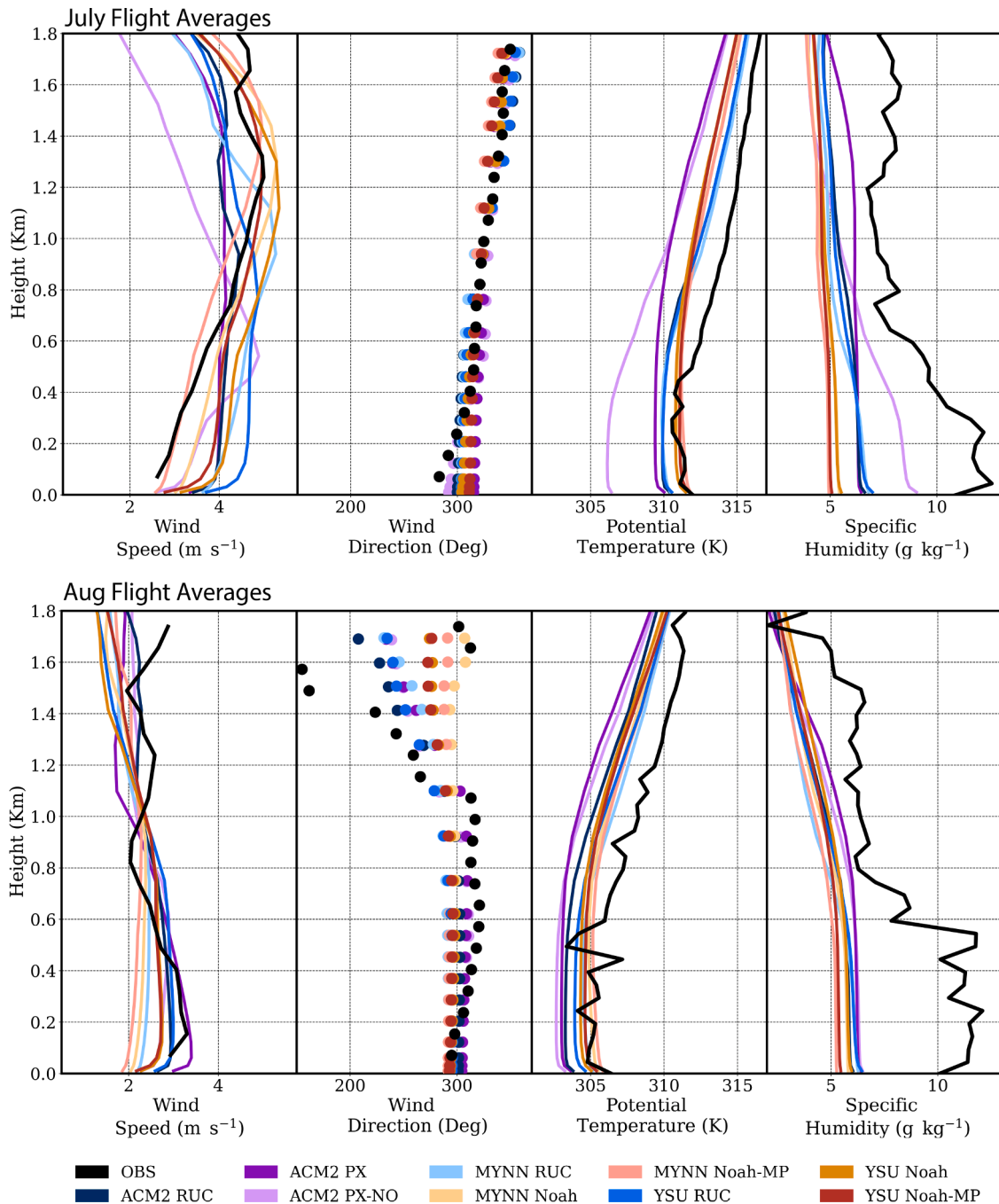


Fig. 7. Daily afternoon (11–16 LST) averaged vertical profiles of wind speed, wind direction, potential temperature and specific humidity for the 27 to 29 July 2016 CABOTS flights (upper panel) and the 4 to 6 August 2016 CABOTS flights (lower panel). Observed vertical wind speed and direction are from the Visalia wind profiler, part of the NOAA ESRL wind profiler network. Observed vertical profiles of potential temperature and specific humidity are averaged over the CABOTS flight region. Dates shown represent the available flight data, and each dataset shows height above ground level.

wind direction profiles are from the Visalia wind profiler and observed profiles potential temperature and specific humidity are averages from the CABOTS flight region when data are available.

No single simulation compares well with the observed vertical distributions of wind speed and direction for both the July and August flight periods. For wind speeds, most simulations are biased high below ≈ 600 m (the approximate PBL height from Fig. 6) in July but conversely, tend to be biased low in August. The observed windspeed profile in August has more of a jet-like shape, which could be argued is somewhat captured by ACM2 PX but with a lower peak. In theory, this could be associated with up-valley flow (toward southern end of the CV), but a low-level jet in this region is usually associated with nocturnal flows (Bao et al., 2008; Caputi et al., 2019). Over both periods in Fig. 7, the YSU model simulations (darker colors) generated higher wind speeds compared to corresponding MYNN simulations for the same LSMs. Hence, during the July period, the MYNN simulations captured the observed wind speed profile magnitude and shape better (especially with Noah-MP), while the YSU model performed better in August (especially with RUC). Focusing again on the PBL region (≈ 600 m and below), vertical wind direction profiles for both periods behave similarly, in that near-surface winds are from the northwest, exhibiting up-valley flow directions as seen by Bao et al. (2008) and Bianco et al. (2011). During the July flights, the upper-level winds continue to smoothly veer north as elevation increases. In contrast, during the August flights, increased variability in the wind direction and veering toward the west is seen above ≈ 1100 m, the approximate height of the coastal mountain range, located west of the wind profiler site (Faloona et al., 2020). This may be associated with a difference in larger-scale meteorology (see Supplemental Materials) and its interactions with the terrain.

The WRF simulations underestimated vertical profiles of specific humidity and potential temperature (with some exceptions discussed below) during both CABOTS flight periods and show more variation by changing the LSM than by changing PBL schemes. In the PBL (up to ≈ 600 m), the observed specific humidity profiles are significantly higher (nearly twice) than those simulated and exhibit a lot more variability. The observed profiles of specific humidity peak a few hundred meters above ground level suggesting some moist air advection, potentially originating with the incoming marine flow (see Figure 11 in Bao et al., 2008). The simulated specific humidity profiles are lower, clustered together and well-mixed suggesting that the modeled soil moisture boundary conditions may be too low throughout the CV and not just at the US-Tw3 Ameriflux site (see Fig. 3). One outlier from the simulated specific humidity profiles is from the July ACM2 PX-NO, which shows some PBL variation that is closer to the observed values but still too dry. July ACM2 PX-NO also correlates with higher LH in the beginning of the analysis period (see Fig. 4). Figure 7 shows that, soil moisture nudging in the ACM2 PX simulation produces worse specific humidity results than PX-NO for the July period and has very little impact in August. Noah and Noah-MP boundary layers were the driest, followed by RUC and PX-based simulations. Simulated profiles of potential temperature invert specific humidity, in that those that performed better for specific humidity, performed worse for potential temperature and vice versa. For instance, Noah and Noah-MP estimate the boundary layer potential temperatures quite well, and the nudging in ACM2 PX does improve potential temperature results, especially for the July period.

PBL depth and structure provide important variables for many applications that rely on WRF simulations. These results show that the differences in the state of the PBL for the CV are largely driven by the LSMs. Therefore, these PBL-scale variables also play an important role for evaluations and new model development of the LSMs. Future work to improve simulations of the PBL for the CV should therefore prioritize improving the LSMs over PBL schemes. Improvements to model initialization would likely also improve the PBL simulations.

3.4. Near-surface meteorological variables

Data from CIMIS stations located throughout the CV (see Fig. 1) were used to generate comprehensive evaluation statistics for near-surface meteorological variables. The Taylor diagram in Fig. 8 shows a comparison of the comprehensive performance statistics for the near-surface meteorology for the nine WRF simulations. Again, this shows that the PBL scheme has much less overall impact on these quantities than the LSM, except for dew point temperatures which show no general trends for LSM or PBL schemes. However, no single LSM outperformed all the others for all variables under all statistical metrics. In general, simulated air temperature (T2) and potential evapotranspiration (ETo) have the best overall statistics. They are highly correlated with observed quantities across the CV ($R \geq 0.9$) and have the lowest RMSE and normalized standard deviations. In this framework, Td2 has the worst performance statistics and is essentially uncorrelated with the observations. Evaluating each simulation's performance depends on the variable and metric of interest. Additional evaluation statistics are presented in Table 6, located in the Supplemental Material.

While the Taylor diagram provides a sense of the overall model performance statistics, diel performance statistics are also useful to evaluate simulation performance. For example, the Taylor diagram shows that T2 exhibits the best model performance, but Fig. 9A shows that all model runs typically have a cool bias that is worst around midnight and a warm bias that peaks around midday by as much as 4°C . In addition, the Taylor diagram (and Table 6 in Supplemental Material) shows that T2 and Td2 model performance improves somewhat through the indirect soil nudging in ACM2 PX versus ACM2 PX-NO. However, the time-series plots show that on shorter time scales, there are many cases for which ACM2 PX has higher bias magnitudes especially during the daytime when the LH is most active. Most simulated cases tend to be biased toward low humidity (Td2) and low wind speeds (WS2), but exhibit diel cycles with \pm biases for both T2 and ETo. The RUC-based simulations typically have the lowest biases for T2, Td2 and WS2, but with a midday ETo bias that is only slightly better than Noah and Noah-MP and notably worse than those from PX and PX-NO.

R_n (see Fig. 4) and the variables in Fig. 9A–C are all used in ETo calculations, and so the biases in the diel cycles of each variable will impact those of ETo. Hence, ETo's strong evaluation statistics in the Taylor Diagram (Fig. 8) may be misleading, and especially so when attempting to correlate with simulated LH. This could point to a stronger dependence (weight) on R_n , which compared relatively well between observations and simulations, in the ETo formulation. Model ETo biases tend to be positive at night and negative during the day when it is most useful for irrigation scheduling, meaning that using these WRF ETo values and a crop coefficient will underestimate the amount of water loss from the surface. Furthermore, Kelley et al. (2020) show that differences between ETo and actual ET in the CV can be significant, especially on daily time scales, even with on-site measurements of meteorological quantities. Such differences in ETo and actual ET are especially important when drought conditions necessitate water conservation and deficit irrigation practices. All of this indicates that despite the strong performance statistics, simulated ETo for the CV may not be a useful practical quantity.

The generally poor comparisons between simulated and measured humidity, low specific humidity profiles in Fig. 7 and negative dew point temperature biases in Fig. 9, suggest that there is not enough water in the overall system, which might be improved with improvements to the soil moisture initialization from NARR. The soil moisture time series comparisons for the US-TW3 site, for which all simulations show significantly lower moisture than measured, help to confirm this assertion. However, point-based soil moisture measurement comparisons with WRF-scale grid cells should be viewed cautiously since using point measurements to represent even plot-scale or flux footprint soil moisture contains inherent uncertainties. In this case though, the correlations between low humidity and low soil moisture, suggest that additional soil

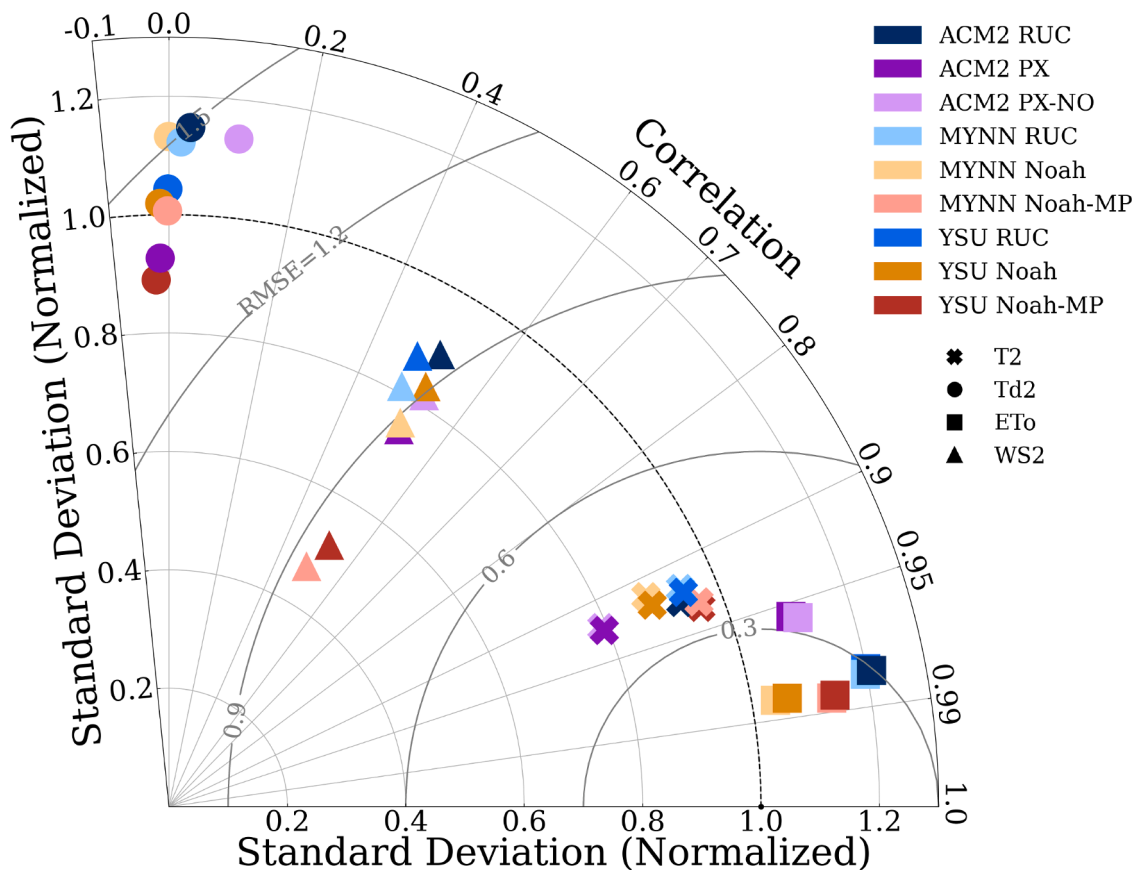


Fig. 8. Taylor diagram showing performance of 2-m air temperature (T2), 2-m dew point temperature (Td2), 2-m wind speed (WS2), and 2-m potential evapotranspiration (Eto), simulated by nine WRF cases compared to observations from 41 CIMIS Stations in the Central Valley.

moisture, to better account for irrigation in the CV, could improve simulations. However, PX-NO, which has drier overall conditions than RUC, Noah and Noah-MP, often performs better for humidity and performs the best overall for LH, with all simulations except PX-NO underestimating LH. This suggests that treatment of the surface fluxes in the LSM also plays an important role in producing high quality humidity estimates near the surface and in the PBL and not just soil moisture magnitudes. In contrast, most of the LSMs perform relatively well for temperatures (Figs. 9 and 7) despite gross overestimations of H, with the exception of PX-NO in the first few days of the study period when it simulates the observed H quite well. These results suggest that while the surface flux partitioning in the energy budget is important, a turbulent flux that is significantly biased can still simulate mean conditions well (e.g., Noah-MP, which has the highest H overestimates, produces good temperature comparisons). It is possible too that the values are ‘right’ for the wrong reasons, however, more flux observations in this region are necessary to confirm these assertions and better understand how the boundary conditions and flux parameterizations relate to atmospheric variables.

Finally, these analyses show that in several variables (most notably, LH, humidity, and PBL height) the indirect soil moisture and temperature nudging in PX appears to produce worse, rather than improved, results compared with PX-NO for which the additional soil nudging does not take place. Temperatures show some minor improvements for PX versus PX-NO, but humidity performance declines between PX and PX-NO is significant, especially during the first five days of the analysis period, or in the top panel of Figs. 7 and in Fig. 9A and B). This effect is partially explained by the WRF assimilated nudging datasets which are hotter and drier compared to independent, in-situ CIMIS observations over cropland. Additional information on the indirect soil nudging is provided in the Supplemental Material Table 5 and Figures 11 and 12.

Since humidity and air temperature are critical components in the PX indirect soil nudging scheme, these discrepancies between the CIMIS observations and the nudging dataset likely cause PX to dry further, and ultimately worsen simulation performance. This implies that the WRF data assimilation products used for the indirect soil moisture nudging in the CV and other arid regions with significant agricultural activities also need developments and should include more direct observations over irrigated croplands. In general, the soil nudging schemes and simulations likely also require better initialization for use in arid regions (see also Pleim and Gilliam, 2009). PX may also need additional model development for arid regions, as it has performed better in extensive testing in the eastern United States (e.g., Gilliam and Pleim, 2010). However, given that the first five days of the simulation show worse comparative statistics for PX than the last five, this may also (or alternatively) indicate that the nudging schemes work better under certain synoptic conditions (see the synoptic conditions in the Supplemental Material) or that arid regions require longer spin-up times for the soil state.

4. Conclusions

Land-atmosphere interactions and boundary layer dynamics over California’s Central Valley (CV) are important for a wide range of applications from agricultural practices to managing and forecasting air quality. Evaluating regional-scale simulations of the CV requires using multi-scale observations of both mean and turbulent quantities because of the range of multi-scale dynamics that occur in this complex marine-valley-mountain system (Bao et al., 2008; Bianco et al., 2011; Faloona et al., 2020). This study compared nine, 15-day, high-resolution WRF simulations that combine various iterations of frequently-used land surface models (LSMs) and planetary boundary layer (PBL) schemes,

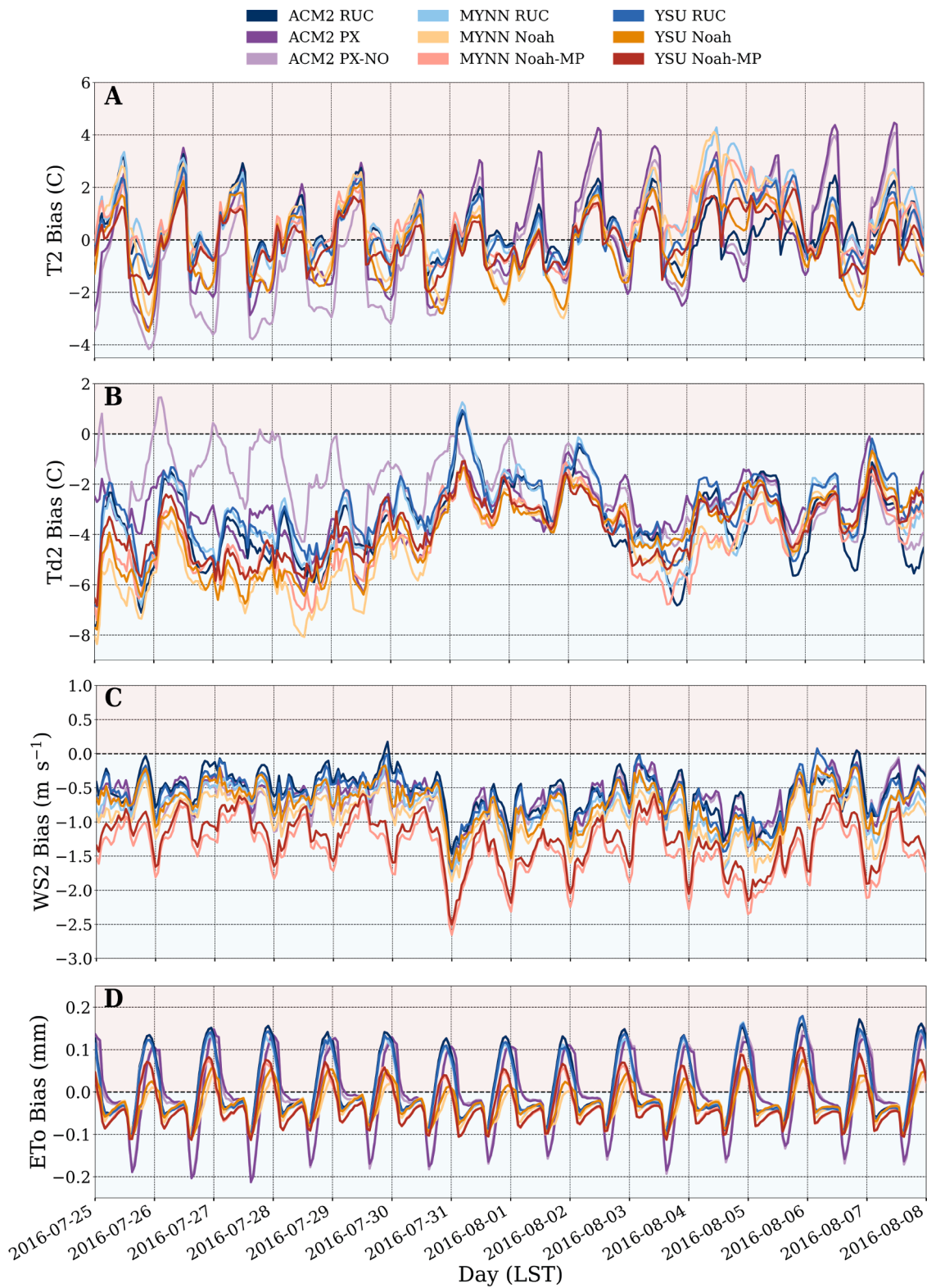


Fig. 9. Hourly time variation of mean biases (MB) using measurements averaged over 41 CIMIS stations in the Central Valley for (A) 2-m air temperature (T2), (B) 2-m dew point temperature (Td2), (C) 2-m wind speed (WS2), and potential evapotranspiration (ETo). Timestamp tick marks indicate midnight.

with a suite of multi-scale observations including near-surface meteorology, surface fluxes, and PBL depth and structure.

An important summarizing result from this study is that changing the PBL scheme resulted in only minor changes to the variables investigated, including PBL structure and height (though it had the most impact on PBL height and PBL wind speeds). Rather the choice of LSM drives most

of the variability between simulations of the boundary layer over the CV for every quantity analyzed. This highlights the importance of the surface state and land-atmosphere coupling in the CV to boundary layer dynamics. The dominating impacts of LSM over PBL scheme choice do, however, contradict test studies for other regions and seasons such as by [Cohen et al. \(2015\)](#).

This study also shows there are some major modeling deficiencies for the CV, and likely for other water-limited regions with similarly arid climates and wide-spread agricultural activities. These WRF results are significantly and negatively impacted by three model aspects. First, our results suggest that soil moisture initializations are too dry, resulting in an insufficient amount of water in the system and leading to exceptionally low humidity. Second, the LSMs show clear deficiencies in simulating sensible heat flux (H) and latent heat flux (LH), and need improvements or new parameterizations for croplands. For example, daytime LH from Noah-MP exhibits nonphysical behavior. It plateaus at values less than 100 Wm^{-2} throughout most of the day (Figs. 4 and 5), and we hypothesize that this is related to problems with the parameterizations for stomatal resistances. Third, air temperatures and humidity from the WRF data assimilation used for indirect nudging in PX are too hot and dry for croplands this region. These assimilation datasets may benefit from improved parameterizations but including more in-situ observations from croplands (e.g., from the CIMIS or other existing agricultural networks) would provide a resource for significant improvements by reducing biases related to irrigation and subsequently, allowing for better evaluations of the model parameterizations. All these problems contribute to biases in the simulated surface H and LH, which drives the simulated PBL dynamics and boundary layer height for the CV (see also Jackson, 2021).

While our study used an unprecedented number of multi-scale observations for the CV, some uncertainty regarding our conclusions remains because available observational data are sparse throughout the region. Another limitation highlighted by this study is a critical need for observations that can be used in WRF initializations and nudging datasets, for model comparisons, and to drive new parameterization developments. Our results also reveal aims for comprehensive, simultaneous and co-located observational strategies and model development, specifically:

- Distributed soil moisture measurements on the scale of the CIMIS network (Fig. 1), or better, would provide important data to quantify both the magnitudes and the heterogeneity of the soil moisture for model comparisons and initializations without relying so heavily on reanalysis or remote sensing products that presently, are too dry for the CV as we have shown. In addition to spatial distribution targeting cropland and other land use patches, we recommend employing standardized depths for soil observations and model outputs to better allow for comparisons with data but also across simulations. These data would also improve our understanding of the physical processes regarding how the soil state impacts micro-meteorology and meteorology at multiple scales. Further, they would inform LSM developments, soil initializations, data assimilation products, and new developments and verifications of satellite remote sensing products such as SMAP.
- Full energy budget, especially surface flux observations, co-located with those of the soil state and boundary layer profiles of wind, temperature, humidity, and ideally, turbulence, are critical to begin to understand land-atmosphere exchange processes and how they impact the larger-scale boundary layer (see also strategies proposed by Wulfmeyer et al., 2018).
- The CIMIS network allowed for a comprehensive analysis of the surface meteorology at several locations across the CV. It is a valuable network, especially for evaluating sub-regional performance differences, for which additional statistical analyses (not shown) suggest may be significant. Bao et al. (2008) found that simulated near-surface winds in different subregions of the CV were more sensitive to different processes e.g., initialization of larger-scale winds or forcing versus the soil states. Hence, a systematic study of land-atmosphere processes and drivers of boundary layer dynamics of the CV must include observational strategies that probe (at a minimum) areas in the Sacramento Valley (northern CV) and the San Joaquin Valley (southern CV). Simultaneously investigating the river

delta where these valleys meet is also suggested as this location in the CV where the marine layer may have the most influence on surface and near-surface conditions.

These observations along with a highly structured, systematic study focused on constraining the soil moisture initialization and boundary condition for irrigated cropland in arid/semi-arid regions and the development and performance of LSMs, like those that have been done in other regions (e.g., Dirmeyer et al., 2018), are necessary for improving regional-scale numerical simulations of the CV and regions with similar climates. Furthermore, sensitivity testing of atmospheric models with improved land-atmosphere coupling would allow for a better understanding of the relative impacts of terrain, soil moisture content, and soil moisture heterogeneity on the simulated PBL dynamics (see also Patton et al., 2005 and Rihani et al., 2015). These improvements would benefit several applications beyond meteorology for the CV, including water use efficiencies for growers (via improved estimates of LH and methodologies for ET_o), state-wide water resource planning under climate change scenarios, chemical transport modeling and air quality studies, and wildfire hazard assessments.

Declaration of Competing Interest

The authors declare the following financial interests/personal relationships which may be considered as potential competing interests:

H. J. Oldroyd reports financial support was provided by National Science Foundation. H. A. Holmes reports financial support was provided by National Science Foundation. X. Sun reports financial support was provided by NOAA Cooperative Agreement with CIRES. I. C. Faloon reports financial support was provided by USDA National Institute of Food and Agriculture and the U.S. Environmental Protection Agency.

Acknowledgements

Data from US-Tw3 used in this study are freely available from Ameriflux (<http://ameriflux.lbl.gov/>). Data from the CIMIS network are located at <https://cimis.water.ca.gov/> and the NOAA Earth System Physical Sciences Laboratory wind profiler data are at <https://psl.noaa.gov/data/obs/datadisply/>. Flight data from the CABOTS project is archived at www.esrl.noaa.gov/csd/projects/cabots. We would like to acknowledge high-performance computing support from Cheyenne (doi:10.5065/D6RX99HX) provided by the University Corporation for Atmospheric Research (NCAR) Computational and Information Systems Laboratory, sponsored by the U.S. National Science Foundation. We additionally thank the anonymous reviewers for their constructive feedback.

Funding: This work was supported by the U.S. National Science Foundation [AGS 1848019] for H.J. Oldroyd, H.A. Holmes was supported by the U.S. National Science Foundation [CBET 2048423], X. Sun was supported in part by the NOAA Cooperative Agreement with CIRES, [NA17OAR4320101], and I.C. Faloon was supported by the USDA National Institute of Food and Agriculture, [Hatch project CA-D-LAW-2481-H]. The CABOTS flight measurements were supported by the U.S. Environmental Protection Agency and Bay Area Air Quality Management District [2016-129], and CABOTS was sponsored by the California Air Resources Board [CARB 14-308]. The authors have no competing interests to declare.

Supplementary material

Supplementary material associated with this article can be found, in the online version, at doi:10.1016/j.agrformet.2022.108898.

References

- Bao, J.W., Michelson, S.A., Persson, P.O., Djalalova, I.V., Wilczak, J.M., 2008. Observed and WRF-simulated low-level winds in a high-ozone episode during the Central California Ozone Study. *J. Appl. Meteorol. Climatol.* <https://doi.org/10.1175/2008JAMC1822.1>.
- Basara, J.B., Christian, J.I., Wakefield, R.A., Otkin, J.A., Hunt, E.H., Brown, D.P., 2019. The evolution, propagation, and spread of flash drought in the Central United States during 2012. *Environ. Res. Lett.* 14 (8), 084025. <https://doi.org/10.1088/1748-9326/ab2cc0>.
- Benjamin, S.G., Grell, G.A., Brown, J.M., Smirnova, T.G., Bleck, R., 2004. Mesoscale weather prediction with the RUC hybrid isentropic–terrain-following coordinate model. *Mon. Weather Rev.* 132 (2), 473–494. [https://doi.org/10.1175/1520-0493\(2004\)132<0473:MWPWTR>2.0.CO;2](https://doi.org/10.1175/1520-0493(2004)132<0473:MWPWTR>2.0.CO;2).
- Berg, A., Lintner, B.R., Findell, K.L., Malyshev, S., Loikith, P.C., Gentine, P., 2014. Impact of soil moisture–atmosphere interactions on surface temperature distribution. *J. Climate* 27 (21), 7976–7993. <https://doi.org/10.1175/JCLI-D-13-00591.1>.
- Bianco, L., Djalalova, I.V., King, C.W., Wilczak, J.M., 2011. Diurnal evolution and annual variability of boundary-layer height and its correlation to other meteorological variables in California's Central Valley. *Boundary-Layer Meteorol.* 140 (3), 491–511. <https://doi.org/10.1007/s10546-011-9622-4>.
- California Department of Water Resources, 2021. California irrigation management information system (CIMIS) website. <https://cimis.water.ca.gov/Resources.aspx>.
- Caputi, D.J., Faloon, I., Trousdell, J., Smoot, J., Falk, N., Conley, S., 2019. Residual layer ozone, mixing, and the nocturnal jet in California's San Joaquin Valley. *Atmos. Chem. Phys.* 19 (7), 4721–4740. <https://doi.org/10.5194/acp-19-4721-2019>. Publisher: Copernicus GmbH.
- Chen, F., Mitchell, K., Schaake, J., Xue, Y., Pan, H.-L., Koren, V., Duan, Q.Y., Ek, M., Betts, A., 1996. Modeling of land surface evaporation by four schemes and comparison with fife observations. *J. Geophys. Res.* 101 (D3), 7251–7268. <https://doi.org/10.1029/95JD02165>.
- Christian, J.I., Basara, J.B., Otkin, J.A., Hunt, E.D., Wakefield, R.A., Flanagan, P.X., Xiao, X., 2019. A methodology for flash drought identification: Application of flash drought frequency across the United States. *J. Hydrometeorol.* <https://doi.org/10.1175/JHM-D-18-0198.1>.
- Cohen, A.E., Cavallo, S.M., Coniglio, M.C., Brooks, H.E., 2015. A review of planetary boundary layer parameterization schemes and their sensitivity in simulating Southeastern U.S. cold season severe weather environments. *Weather Forecast.* <https://doi.org/10.1175/waf-d-14-00105.1>.
- Dieter, C.A., Maupin, M.A., Caldwell, R.R., Harris, M.A., Ivahnenko, T.I., Lovelace, J.K., Barber, N.L., Linsey, K.S., 2018. Estimated Use of Water in the United States in 2015. Technical Report. U. S. Geological Survey, Reston, VA. <https://doi.org/10.3133/cir1441>.
- Dirmeyer, P.A., Chen, L., Wu, J., Shin, C.-S., Huang, B., Cash, B.A., Bosilovich, M.G., Mahanama, S., Koster, R.D., Santanello, J.A., Ek, M.B., Balsamo, G., Dutra, E., Lawrence, D.M., 2018. Verification of land–atmosphere coupling in forecast models, reanalyses, and land surface models using flux site observations. *J. Hydrometeorol.* 19 (2), 375–392. <https://doi.org/10.1175/JHM-D-17-0152.1>. Publisher: American Meteorological Society Section: Journal of Hydrometeorology.
- Dirmeyer, P.A., Halder, S., 2016. Sensitivity of numerical weather forecasts to initial soil moisture variations in CFSv2. *Weather Forecast.* 31 (6), 1973–1983. <https://doi.org/10.1175/WAF-D-16-0049.1>.
- Dong, A., Grattan, S.R., Carroll, J.J., Prashar, C.R.K., 1992. Estimation of daytime net radiation over well-watered grass. *J. Irrig. Drain. Eng.* 118 (3), 466–479. [https://doi.org/10.1061/\(ASCE\)0733-9437\(1992\)118:3\(466\)](https://doi.org/10.1061/(ASCE)0733-9437(1992)118:3(466)).
- Ek, M.B., Holtslag, A.A.M., 2004. Influence of soil moisture on boundary layer cloud development. *J. Hydrometeorol.* 5 (1), 86–99. [https://doi.org/10.1175/1525-7541\(2004\)005<0086:IOSMOB>2.0.CO;2](https://doi.org/10.1175/1525-7541(2004)005<0086:IOSMOB>2.0.CO;2).
- Ek, M.B., Mitchell, K.E., Lin, Y., Rogers, E., Grunmann, P., Koren, V., Gayno, G., Tarpley, J.D., 2003. Implementation of Noah land surface model advances in the national centers for environmental prediction operational mesoscale Eta model. *J. Geophys. Res.* 108 (D22) <https://doi.org/10.1029/2002JD003296>.
- Faloon, I.C., Chiao, S., Eiserloh, A.J., Alvarez, R.J., Kirgis, G., Langford, A.O., Senff, C.J., Caputi, D., Hu, A., Iraci, L.T., Yates, E.L., Marrero, J.E., Ryo, J.-M., Conley, S., Tanrikulu, S., Xu, J., Kuwayama, T., 2020. The California baseline ozone transport study (CABOTS). *Bull. Am. Meteorol. Soc.* 101 (4), E427–E445. <https://doi.org/10.1175/BAMS-D-18-0302.1>. Publisher: American Meteorological Society Section: Bulletin of the American Meteorological Society.
- Fan, Y., van den Dool, H.M., Wu, W., 2011. Verification and intercomparison of multimodel simulated land surface hydrological datasets over the United States. *J. Hydrometeorol.* 12 (4), 531–555. <https://doi.org/10.1175/2011JHM1317.1>.
- Faunt, C.C., Sneed, M., Traum, J., Brandt, J.T., 2016. Water availability and land subsidence in the Central Valley, California, USA. *Hydrogeol. J.* 24 (3), 675–684. <https://doi.org/10.1007/s10040-015-1339-x>.
- Fernando, D.N., Mo, K.C., Fu, R., Pu, B., Bowerman, A., Scanlon, B.R., Solis, R.S., Yin, L., Mace, R.E., Mioduszewski, J.R., Ren, T., Zhang, K., 2016. What caused the spring intensification and winter demise of the 2011 drought over Texas? *Climate Dyn.* 47 (9), 3077–3090. <https://doi.org/10.1007/s00382-016-3014-x>.
- Ford, T.W., Rapp, A.D., Quiring, S.M., 2015. Does afternoon precipitation occur preferentially over dry or wet soils in Oklahoma? *J. Hydrometeorol.* 16 (2), 874–888. <https://doi.org/10.1175/JHM-D-14-0005.1>.
- Gevaert, A., Gonzalez Miralles, D., de Jeu, R., Schellekens, J., Dolman, A., 2018. Soil moisture–temperature coupling in a set of land surface models. *J. Geophys. Res.* 123 (3), 1481–1498. <https://doi.org/10.1002/2017JD027346>.
- Gilliam, R.C., Pleim, J.E., 2010. Performance assessment of new land surface and planetary boundary layer physics in the WRF-ARW. *J. Appl. Meteorol. Climatol.* 49 (4), 760–774. <https://doi.org/10.1175/2009JAMC2126.1>.
- Guilod, B.P., Orłowsky, B., Miralles, D.G., Teuling, A.J., Seneviratne, S.I., 2015. Reconciling spatial and temporal soil moisture effects on afternoon rainfall. *Nat. Commun.* 6 (1), 6443. <https://doi.org/10.1038/ncomms7443>. Bandiera_abtest: a Cc license type: cc by Cg type: Nature Research Journals Number: 1 Primary type: Research Publisher: Nature Publishing Group Subject term: Atmospheric science; Climate-change impacts Subject term id: atmospheric-science;climate-change-impacts
- Hohenegger, C., Brockhaus, P., Bretherton, C.S., Schär, C., 2009. The soil moisture–precipitation feedback in simulations with explicit and parameterized convection. *J. Climate* 22 (19), 5003–5020. <https://doi.org/10.1175/2009JCLI2604.1>. Publisher: American Meteorological Society Section: Journal of Climate.
- Hong, S.-Y., Noh, Y., Dudhia, J., 2006. A new vertical diffusion package with an explicit treatment of entrainment processes. *Mon. Weather Rev.* 134 (9), 2318–2341. <https://doi.org/10.1175/MWR3199.1>.
- Huang, X., Ullrich, P.A., 2016. Irrigation impacts on California's climate with the variable-resolution CESM. *J. Adv. Model. Earth Syst.* 8 (3), 1151–1163. <https://doi.org/10.1002/2016MS000656>.
- Jackson, B., 2021. Simulating summer mixing heights in California's San Joaquin Valley using the WRF meteorological model with three land surface modules. *Meteorol. Atmos. Phys.* 133 (3), 925–942. <https://doi.org/10.1007/s00703-021-00786-1>.
- Jiménez, P.A., Dudhia, J., González-Rouco, J.F., Navarro, J., Montávez, J.P., García-Bustamante, E., 2012. A revised scheme for the WRF surface layer formulation. *Mon. Weather Rev.* 140 (3), 898–918. <https://doi.org/10.1175/MWR-D-11-00056.1>.
- Kala, J., Evans, J.P., Pitman, A.J., 2015. Influence of antecedent soil moisture conditions on the synoptic meteorology of the Black Saturday bushfire event in southeast Australia. *Q. J. R. Meteorol. Soc.* 141 (693), 3118–3129. <https://doi.org/10.1002/qj.2596>.
- Kelley, J., McCauley, D., Alexander, G.A., Gray, W.F., Siegfried, R., Oldroyd, H.J., 2020. Using machine learning to integrate on-farm sensors and agro-meteorology networks into site-specific decision support. *Trans. ASABE* 63 (5), 1427–1439. <https://doi.org/10.13031/trans.13917>.
- Koster, R.D., Dirmeyer, P.A., Guo, Z., Bonan, G., Chan, E., Cox, P., Gordon, C.T., Kanae, S., Kowalczyk, E., Lawrence, D., Liu, P., Lu, C.-H., Malyshev, S., McAvaney, B., Mitchell, K., Mocko, D., Oki, T., Oleson, K., Pitman, A., Sud, Y.C., Taylor, C.M., Verseghy, D., Vasic, R., Xue, Y., Yamada, T., 2004. Regions of strong coupling between soil moisture and precipitation. *Science* 305 (5687), 1138–1140. <https://doi.org/10.1126/science.1100217>.
- Koster, R.D., Reichle, R.H., Schubert, S.D., Mahanama, S.P., 2019. Length scales of hydrological variability as inferred from SMAP soil moisture retrievals. *J. Hydrometeorol.* 20 (11), 2129–2146. <https://doi.org/10.1175/JHM-D-19-0070.1>.
- Kueppers, L.M., Snyder, M.A., 2012. Influence of irrigated agriculture on diurnal surface energy and water fluxes, surface climate, and atmospheric circulation in California. *Climate Dyn.* 38 (5), 1017–1029. <https://doi.org/10.1007/s00382-011-1123-0>.
- Langford, A.O., Alvarez II, R.J., Brioude, J., Caputi, D., Conley, S.A., Evan, S., Faloon, I.C., Iraci, L.T., Kirgis, G., Marrero, J.E., Ryo, J.-M., Senff, C.J., Yates, E.L., 2020. Ozone production in the Soberanes smoke haze: implications for air quality in the San Joaquin Valley during the California baseline ozone transport study. *J. Geophys. Res.* 125 (11) <https://doi.org/10.1029/2019JD031777>.
- Lawston, P.M., Santanello Jr, J.A., Kumar, S.V., 2017. Irrigation signals detected from SMAP soil moisture retrievals. *Geophys. Res. Lett.* 44 (23), 11,860–11,867. <https://doi.org/10.1002/2017GL075733>.
- Leeper, R.D., Bell, J.E., Vines, C., Palecki, M., 2017. An evaluation of the North American regional reanalysis simulated soil moisture conditions during the 2011–13 drought period. *J. Hydrometeorol.* 18 (2), 515–527. <https://doi.org/10.1175/JHM-D-16-0132.1>.
- Lin, Y.-L., Jao, I.-C., 1995. A numerical study of flow circulations in the Central Valley of California and formation mechanisms of the Fresno Eddy. *Mon. Weather Rev.* 123 (11), 3227–3239. [https://doi.org/10.1175/1520-0493\(1995\)123<3227:ANSOFC>2.0.CO;2](https://doi.org/10.1175/1520-0493(1995)123<3227:ANSOFC>2.0.CO;2).
- Lo, M.-H., Famiglietti, J.S., 2013. Irrigation in California's Central Valley strengthens the southwestern U.S. water cycle. *Geophys. Res. Lett.* 40 (2), 301–306. <https://doi.org/10.1002/grl.50108>.
- Mesinger, F., DiMego, G., Kalnay, E., Mitchell, K., Shafran, P.C., Ebisuzaki, W., Jović, D., Woollen, J., Rogers, E., Berbery, E.H., Ek, M.B., Fan, Y., Grumbine, R., Higgins, W., Li, H., Lin, Y., Manikin, G., Parrish, D., Shi, W., 2006. North American regional reanalysis. *Bull. Am. Meteorol. Soc.* 87 (3), 343–360. <https://doi.org/10.1175/BAMS-87-3-343>.
- Michelson, S.A., Bao, J.-W., 2008. Sensitivity of low-level winds simulated by the WRF model in California's Central Valley to uncertainties in the large-scale forcing and soil initialization. *J. Appl. Meteorol. Climatol.* 47 (12), 3131–3149. <https://doi.org/10.1175/2008JAMC1782.1>.
- Milovac, J., Warrach-Sagi, K., Behrendt, A., Späth, F., Ingwersen, J., Wulfmeyer, V., 2016. Investigation of PBL schemes combining the WRF model simulations with scanning water vapor differential absorption lidar measurements. *J. Geophys. Res.* 121 (2), 624–649. <https://doi.org/10.1002/2015JD023927>.
- Nakanishi, M., Niino, H., 2004. An improved Mellor–Yamada level-3 model with condensation physics: its design and verification. *Boundary-Layer Meteorol.* <https://doi.org/10.1023/B:BOUN.0000020164.04146.98>.
- Nakanishi, M., Niino, H., 2009. Development of an improved turbulence closure model for the atmospheric boundary layer. *J. Meteorol. Soc. Jpn.* Ser. II 87 (5), 895–912. <https://doi.org/10.2151/jmsj.87.895>.

- Ning, Z., Williams, Q.L., Heping, L., 2010. Effects of land-surface heterogeneity on numerical simulations of mesoscale atmospheric boundary layer processes. *Theor. Appl. Climatol.* 102 (3–4), 307–317. <https://search.ebscohost.com/login.aspx?direct=true&db=a9h&AN=55052263&site=ehost-live>.
- Niu, G.-Y., Yang, Z.-L., Mitchell, K.E., Chen, F., Ek, M.B., Barlage, M., Kumar, A., Manning, K., Niyogi, D., Rosero, E., Tewari, M., Xia, Y., 2011. The community Noah land surface model with multiparameterization options (Noah-MP): 1. Model description and evaluation with local-scale measurements. *J. Geophys. Res.* 116 (D12) <https://doi.org/10.1029/2010JD015139>.
- NOAA/NCEP 2004, 2004a. NCEP ADP Global Surface Observational Weather Data, October 1999 - continuing. <https://doi.org/10.5065/4F4P-E398>.
- NOAA/NCEP 2004, 2004b. NCEP ADP Global Upper Air Observational Weather Data, October 1999 - continuing. <https://doi.org/10.5065/39C5-Z211>.
- Noilhan, J., Planton, S., 1989. A simple parameterization of land surface processes for meteorological models. *Mon. Weather Rev.* 117 (3), 536–549. [https://doi.org/10.1175/1520-0493\(1989\)117<0536:ASPOLS>2.0.CO;2](https://doi.org/10.1175/1520-0493(1989)117<0536:ASPOLS>2.0.CO;2).
- Oikawa, P., Sturtevant, C., Knox, S., Verfaillie, J., Huang, Y., Baldocchi, D., 2017. Revisiting the partitioning of net ecosystem exchange of CO₂ into photosynthesis and respiration with simultaneous flux measurements of 13CO₂ and CO₂, soil respiration and a biophysical model. *CANVEG. Agric. Forest Meteorol.* 234–235, 149–163. <https://doi.org/10.1016/j.agrformet.2016.12.016>.
- O'Neill, P. E., Chan, S., Njoku, E. G., Jackson, T., Bindlish, R., 2019. SMAP Enhanced L3 Radiometer global daily 9 km EASE-Grid soil moisture, version 3. <https://doi.org/10.5067/T90W6VRLCBHI>.
- Patton, E.G., Sullivan, P.P., Moeng, C.-H., 2005. The influence of idealized heterogeneity on wet and dry planetary boundary layers coupled to the land surface. *J. Atmos. Sci.* 62 (7), 2078–2097. <https://doi.org/10.1175/JAS3465.1>. Publisher: American Meteorological Society Section: Journal of the Atmospheric Sciences.
- Pleim, J.E., 2006. A simple, efficient solution of flux–profile relationships in the atmospheric surface layer. *J. Appl. Meteorol. Climatol.* 45 (2), 341–347. <https://doi.org/10.1175/JAM2339.1>.
- Pleim, J.E., 2007. A combined local and nonlocal closure model for the atmospheric boundary layer. part i: Model description and testing. *J. Appl. Meteorol. Climatol.* 46 (9), 1383–1395. <https://doi.org/10.1175/JAM2539.1>.
- Pleim, J.E., 2007. A combined local and nonlocal closure model for the atmospheric boundary layer. part ii: Application and evaluation in a mesoscale meteorological model. *J. Appl. Meteorol. Climatol.* 46 (9), 1396–1409. <https://doi.org/10.1175/JAM2534.1>.
- Pleim, J.E., Gilliam, R., 2009. An indirect data assimilation scheme for deep soil temperature in the Pleim–Xiu land surface model. *J. Appl. Meteorol. Climatol.* 48 (7), 1362–1376. <https://doi.org/10.1175/2009JAMC2053.1>.
- Pleim, J.E., Xiu, A., 2003. Development of a land surface model. Part II: data assimilation. *J. Appl. Meteorol.* 42 (12), 1811–1822. [https://doi.org/10.1175/1520-0450\(2003\)042<1811:DOALSM>2.0.CO;2](https://doi.org/10.1175/1520-0450(2003)042<1811:DOALSM>2.0.CO;2).
- Pruitt, W.O., Doorenbos, J., 1977. Empirical calibration: a requisite for evapotranspiration formulae based on daily or longer mean climate data? ICID Conference on Evapotranspiration. International Commission on Irrigation and Drainage, pp. 1–10.
- Ran, L., Gilliam, R., Binkowski, F.S., Xiu, A., Pleim, J., Band, L., 2015. Sensitivity of the weather research and forecast/community multiscale air quality modeling system to MODIS LAI, FPAR, and albedo. *J. Geophys. Res.* 120 (16), 8491–8511. <https://doi.org/10.1002/2015JD023424>.
- Ran, L., Pleim, J., Gilliam, R., Binkowski, F.S., Hogrefe, C., Band, L., 2016. Improved meteorology from an updated WRF/CSMAQ modeling system with MODIS vegetation and albedo. *J. Geophys. Res.* 121 (5), 2393–2415. <https://doi.org/10.1002/2015JD024406>.
- Reichle, R., Lannoy, G. D., Koster, R. D., Crow, W. T., Kimball, J. S., Liu, Q., 2018. SMAP L4 global 9 km EASE-grid surface and root zone soil moisture land model constants, version 4. <https://doi.org/10.5067/KGLC3UH4TMAQ>.
- Richards, L.A., 1931. Capillary conduction of liquids through porous mediums. *Physics* 1 (5), 318–333. <https://doi.org/10.1063/1.1745010>.
- Rihani, J.F., Chow, F.K., Maxwell, R.M., 2015. Isolating effects of terrain and soil moisture heterogeneity on the atmospheric boundary layer: idealized simulations to diagnose land-atmosphere feedbacks. *J. Adv. Model. Earth Syst.* 7 (2), 915–937. <https://doi.org/10.1002/2014MS000371>.
- Santanello, J.A., Dirmeyer, P.A., Ferguson, C.R., Findell, K.L., Tawfik, A.B., Berg, A., Ek, M., Gentile, P., Guillod, B.P., Van Heerwaarden, C., Roundy, J., Wulfmeyer, V., 2018. Land-atmosphere interactions the LoCo perspective. *Bull. Am. Meteorol. Soc.* 99 (6), 1253–1272. <https://doi.org/10.1175/BAMS-D-17-0001.1>.
- Santanello, J.A., Friedl, M.A., Ek, M.B., 2007. Convective planetary boundary layer interactions with the land surface at diurnal time scales: Diagnostics and feedbacks. *J. Hydrometeorol.* 8 (5), 1082–1097. <https://doi.org/10.1175/JHM614.1>.
- Santanello, J.A., Peters-Lidard, C.D., Kumar, S.V., 2011. Diagnosing the sensitivity of local land-atmosphere coupling via the soil moisture–boundary layer interaction. *J. Hydrometeorol.* 12 (5), 766–786. <https://doi.org/10.1175/JHM-D-10-05014.1>.
- Santanello Jr., J.A., Lawston, P., Kumar, S., Dennis, E., 2019. Understanding the impacts of soil moisture initial conditions on NWP in the context of land–atmosphere coupling. *J. Hydrometeorol.* 20 (5), 793–819. <https://doi.org/10.1175/JHM-D-18-0186.1>.
- Sathyanadh, A., Prabha, T.V., Balaji, B., Resmi, E., Karipot, A., 2017. Evaluation of WRF PBL parameterization schemes against direct observations during a dry event over the Ganges Valley. *Atmos. Res.* 193, 125–141. <https://doi.org/10.1016/j.atmosres.2017.02.016>.
- Schwingshackl, C., Hirschi, M., Seneviratne, S.I., 2017. Quantifying spatiotemporal variations of soil moisture control on surface energy balance and near-surface air temperature. *J. Climate* 30 (18), 7105–7124. <https://doi.org/10.1175/JCLI-D-16-0727.1>.
- Skamarock, W.C., Wang, W., Klemp, J.B., Dudhia, J., Gill, D.O., Barker, D.M., Duda, M. G., Huang, X.-y., Powers, J.G., 2008. 2005: A Description of the Advanced Research WRF Version 3. NCAR Tech Note. <https://doi.org/10.5065/D6DZ069T>.
- Smirnova, T.G., Brown, J.M., Benjamin, S.G., 1997. Performance of different soil model configurations in simulating ground surface temperature and surface fluxes. *Mon. Weather Rev.* 125 (8), 1870–1884. [https://doi.org/10.1175/1520-0493\(1997\)125<1870:PODSMC>2.0.CO;2](https://doi.org/10.1175/1520-0493(1997)125<1870:PODSMC>2.0.CO;2).
- Smirnova, T.G., Brown, J.M., Benjamin, S.G., Kenyon, J.S., 2015. Modifications to the rapid update cycle land surface model (RUC LSM) available in the weather research and forecasting (WRF) model. *Mon. Weather Rev.* <https://doi.org/10.1175/mwr-d-15-0198.1>.
- Sorooshian, S., AghaKouchak, A., Li, J., 2014. Influence of irrigation on land hydrological processes over California. *J. Geophys. Res.* 119 (23), 13,137–13,152. <https://doi.org/10.1002/2014JD022232>.
- Sorooshian, S., Li, J., Hsu, K.-I., Gao, X., 2011. How significant is the impact of irrigation on the local hydroclimate in California's Central Valley? Comparison of model results with ground and remote-sensing data. *J. Geophys. Res.* 116 (D6) <https://doi.org/10.1029/2010JD014775>.
- Sorooshian, S., Li, J., Hsu, K.-I., Gao, X., 2012. Influence of irrigation schemes used in regional climate models on evapotranspiration estimation: results and comparative studies from California's Central Valley agricultural regions. *J. Geophys. Res.* 117 (D6) <https://doi.org/10.1029/2011JD016978>.
- Stull, R.B., 1988. *An Introduction to Boundary Layer Meteorology*, vol. 13. Springer Netherlands, Dordrecht. <https://doi.org/10.1007/978-94-009-3027-8>.
- Sun, X., Holmes, H.A., Osibanjo, O.O., Sun, Y., Ivey, C.E., 2017. Evaluation of surface fluxes in the WRF model: case study for farmland in rolling terrain. *Atmosphere* 8 (10). <https://doi.org/10.3390/atmos8100197>.
- Trousdell, J.F., Caputi, D., Smoot, J., Conley, S.A., Faloon, I.C., 2019. Photochemical production of ozone and emissions of NO_x and CH₄ in the San Joaquin Valley. *Atmos. Chem. Phys.* 19 (16), 10697–10716. <https://doi.org/10.5194/acp-19-10697-2019>.
- Van Den Broeke, M.S., Kalin, A., Alavez, J.A.T., Oglesby, R., Hu, Q., 2018. A warm-season comparison of WRF coupled to the CLM4.0, Noah-MP, and Bucket hydrology land surface schemes over the Central USA. *Theor. Appl. Climatol.* 134 (3), 801–816. <https://doi.org/10.1007/s00704-017-2301-8>.
- Welty, J., Zeng, X., 2018. Does soil moisture affect warm season precipitation over the Southern Great Plains? *Geophys. Res. Lett.* 45 (15), 7866–7873. <https://doi.org/10.1029/2018GL078598>.
- Wulfmeyer, V., Turner, D.D., Baker, B., Banta, R., Behrendt, A., Bonin, T., Brewer, W.A., Buban, M., Choukulkar, A., Dumas, E., Hardesty, R.M., Heus, T., Ingwersen, J., Lange, D., Lee, T.R., Metzendorf, S., Muppa, S.K., Meyers, T., Newsom, R., Osman, M., Raasch, S., Santanello, J., Senff, C., Späth, F., Wagner, T., Weckwerth, T., 2018. A new research approach for observing and characterizing land–atmosphere feedback. *Bull. Am. Meteorol. Soc.* 99 (8), 1639–1667. <https://doi.org/10.1175/BAMS-D-17-0009.1>.
- Wyngaard, J., 2010. *Turbulence in the Atmosphere*. Cambridge University Press.
- Xia, Y., Ek, M.B., Wu, Y., Ford, T., Quiring, S.M., 2015. Comparison of NLDAS-2 simulated and NASMD observed daily soil moisture. Part I: comparison and analysis. *J. Hydrometeorol.* 16 (5), 1962–1980. <https://doi.org/10.1175/JHM-D-14-0096.1>.
- Xiu, A., Pleim, J.E., 2001. Development of a land surface model. Part I: application in a mesoscale meteorological model. *J. Appl. Meteorol.* 40 (2), 192–209. [https://doi.org/10.1175/1520-0450\(2001\)040<0192:DOALSM>2.0.CO;2](https://doi.org/10.1175/1520-0450(2001)040<0192:DOALSM>2.0.CO;2).
- Xu, L., Pyles, R.D., U, K.T.P., Snyder, R., Monier, E., Falk, M., Chen, S.-H., 2017. Impact of canopy representations on regional modeling of evapotranspiration using the WRF-ACASA coupled model. *Agric. Forest Meteorol.* 247, 79–92. <https://doi.org/10.1016/j.agrformet.2017.07.003>.
- Yang, Z., Qian, Y., Liu, Y., Berg, L.K., Hu, H., Dominguez, F., Yang, B., Feng, Z., Gustafson Jr, W.I., Huang, M., Tang, Q., 2019. Irrigation impact on water and energy cycle during dry years over the United States using convection-permitting WRF and a dynamical recycling model. *J. Geophys. Res.* 124 (21), 11220–11241. <https://doi.org/10.1029/2019JD030524>.
- Yang, Z.-L., Niu, G.-Y., Mitchell, K.E., Chen, F., Ek, M.B., Barlage, M., Longuevergne, L., Manning, K., Niyogi, D., Tewari, M., Xia, Y., 2011. The community Noah land surface model with multiparameterization options (Noah-MP): 2. Evaluation over global river basins. *J. Geophys. Res.* 116 (D12) <https://doi.org/10.1029/2010JD015140>.
- Zaitchik, B.F., Santanello, J.A., Kumar, S.V., Peters-Lidard, C.D., 2013. Representation of soil moisture feedbacks during drought in NASA Unified WRF (NU-WRF). *J. Hydrometeorol.* 14 (1), 360–367. <https://doi.org/10.1175/JHM-D-12-069.1>.
- Zhang, J., Wang, W.-C., Wei, J., 2008. Assessing land-atmosphere coupling using soil moisture from the global land data assimilation system and observational precipitation. *J. Geophys. Res.* 113 (D17) <https://doi.org/10.1029/2008JD009807>.
- Zhang, Y., Gao, Z., Li, D., Li, Y., Zhang, N., Zhao, X., Chen, J., 2014. On the computation of planetary boundary-layer height using the bulk Richardson number method. *Geosci. Model Dev.* 7 (6), 2599–2611. <https://doi.org/10.5194/gmd-7-2599-2014>.
- Zhang, Z., Barlage, M., Chen, F., Li, Y., Helgason, W., Xu, X., Liu, X., Li, Z., 2020. Joint modeling of crop and irrigation in the central United States using the Noah-MP land surface model. *J. Adv. Model. Earth Syst.* 12 (7) <https://doi.org/10.1029/2020MS002159>.